Departamento de Física

Universidade de Aveiro

Ano 2018-2019

Jorge Pedro Amaral Duarte de Moura

Development of an inductive heating system for the graphene synthesis by cold wall CVD

Desenvolvimento de um sistema de aquecimento indutivo para a síntese de grafeno por CVD em reator de parede fria

Universidade de Aveiro

Departamento de Física

Ano 2018-2019

Jorge Pedro Amaral Duarte de Moura

Development of an inductive heating system for the graphene synthesis by cold wall CVD

Desenvolvimento de um sistema de aquecimento indutivo para a síntese de grafeno por CVD em reator de parede fria

Dissertação apresentada à Universidade de Aveiro para cumprimento dos requisitos necessários à obtenção do grau de Mestre em engenharia Física, realizada sob a orientação científica Doutora Florinda Mendes da Costa, Professora Associada do Departamento de Física da Universidade de Aveiro, do Doutor João Pedro Estima de Oliveira, Professor Associado do Departamento de Eletrónica e Telecomunicações da Universidade de Aveiro e António José Silva Fernandes, Técnico Superior do Departamento de Física da Universidade de Aveiro

Trabalho desenvolvido no âmbito do projeto UID/CTM/50015/2019 financiado por fundos nacionais pela FCT/MEC (UID/CTM/50025/2019) e cofinanciado pelo FEDER(POCI-01-0145-FEDER028755) sob o acordo de parceria PT2020.

Dedico este trabalho a quem teve paciência de mo ver fazer, ao conhecimento como motor de desenvolvimento humano

o júri

presidente

Prof. Doutor Luís Miguel Rino Cerveira da Silva
professor auxiliar da Universidade de Aveiro

Prof. Doutor Florinda Mendes da Costa
professor associado da Universidade de Aveiro

Prof. Doutor Carlos José Tavares
professor auxiliar do departamento de Física da Universidade do Minho

agradecimentos

Agradeço a todos os que de forma directa ou indirecta me ajudaram, quer com os seus inputs científicos como motivacionais durante as diferentes etapas deste projecto. Saliento que seria impossível ter chegado a esta conclusão sem a sua presença.

palavras-chave

Grafeno; Deposição Química em Fase de Vapor; Reator de Parede Fria; COMSOL; Indução Electromagnética; Pirometria Ótica

resumo

Desde que foi isolado pela primeira vez, o grafeno assumiu-se como um dos nano-materiais mais investigados dadas as suas extraordinárias propriedades, nomeadamente a condução elétrica quase balística e elevada mobilidade de carga, transparência ótica e comportamento mecânico extremo, compatíveis com um sem número de campos de aplicação. No entanto, a sua produção industrial em larga escala ainda não foi alcançada, e vários métodos de síntese foram sendo desenvolvidos num esforço para atingir esse objetivo. A síntese rápida, controlada e escalável num processo contínuo de grafeno monocristalino são condições altamente desejáveis que a técnica de Deposição Química em Fase de Vapor oferece.

Este trabalho baseia-se no desenvolvimento de um sistema de aquecimento indutivo para a síntese de grafeno num reator CVD de parede fria, englobando a sua conceção, construção e validação. Esta abordagem permitiu obter curvas de aquecimento rápidas e controladas, numa configuração de amostra suspensa, possibilitando uma operação baseada na monitorização pirométrica da temperatura como parâmetro chave para o processo de crescimento. Utilizando este equipamento, foi possível obter domínios hexagonais de grafeno de camada única e elevada qualidade, como confirmado por espectroscopia de Raman e microscopia eletrónica de varrimento.

O presente trabalho contribui para a compreensão dos mecanismos de crescimento de grafeno através do controlo preciso da temperatura do substrato, identificado como um parâmetro chave.

keywords

Graphene; Chemical Vapour Deposition; Cold Wall Reactor; COMSOL; Electromagnetic Induction; Optical Pyrometry.

abstract

Since it was firstly isolated, graphene has become one of the most researched nano materials, due to its exciting physical and chemical properties, namely the nearly ballistic transport and high charge mobility, optical transparency and extreme mechanical behaviour, meeting a plethora of application fields. However, the industrial mass-production is still to overcome, and a multitude of growing processes evolved as an effort to reach this objective. Fast, controlled and scalable growth of single crystalline graphene in a continuous process are the basic guidelines for an ideal synthesis process, that the Chemical Vapour Deposition (CVD) technique can offer.

This work settles on the exploitation of Cold Wall CVD by designing, developing and testing an electromagnetic inductively assisted CVD system. This approach proved to enable rapid and controlled heating curves, allowing for sample suspension inside the reactor tube, permitting an operation based on optical pyrometric monitoring of the temperature as a key parameter for the growth process. Using this system, high quality single layer graphene domains with well-defined hexagonal shape were obtained, as confirmed by Raman spectroscopy and scanning electron microscopy.

The present work contributes with an effort towards an understanding of graphene growth mechanisms in order to accurately control the substrate temperature, a key growth parameter.

Contents

List of Figures

List of Tables

List of Abbreviations

AC – Alternate Current

BC – Boundary Conditions

CNC – Computer Numeric Control

CWCVD – Cold Wall Chemical Vapour Deposition

DC – Direct Current

OP – Operational Amplifier

GB – Grain Boundaries

Gr – Graphene

GrD – Graphene Domain

h-BN – Hexagonal Boron Nitride

IGBT – Insulated-Gate Bipolar Transistor

IHCVD – Induction Heating Chemical Vapour Deposition

RLC – Resistive, Inductive (L), Capacitive

SEM – scanning Electron Microscope

SLG – Single Layer Graphene

PA – Power Amplifier

PD – Pulsed Deposition

PID – Primitive Integral Derivative (Control function)

PLL – Phase Locked Loop

VDR – Voltage Doubler Rectifier

TCVD – Thermal Chemical Vapour Deposition

I. Introductory themes

1. Introduction

Graphene, is a two-dimensional, single-layer sheet of sp2 hybridized carbon atoms, with highly attractive physical properties as large carrier mobilities (up to 200000 $cm^2V^{-1}s^{-1}$) and ballistic transport distances of up to a micron at room temperature make it potentially useful for high frequency electronic devices, while the low absorbance (2.3% of visible light) complemented with its semi-metallic nature makes it an ideal transparent conductor where transparency and low resistance are required

Chemical vapor deposition (CVD) has been considered the most promising technique for producing high-quality and large-area graphene. The most widely used substrate for the CVD growth of graphene is Cu. The surface reaction mechanism is advantageous for the synthesis of monolayer graphene. Investigation of metal-catalysed CVD has shown that parameters such as temperature, pressure, substrate, and precursor concentration, strongly dictate graphene growth mechanisms.

2. Main reactor types

In the search of pristine graphene growth in CVD conditions, different practical approaches were explored in the literature. Thermal Chemical Vapor Deposition reactors (TCVD) and Graphene (Gr) deposition in Cold Wall CVD (CWCVD), represent two reactor family groups with different characteristics related with thermal source and temperature distribution inside the deposition zone. Other ramifications can be included, as pressure (Low, Middle and Atmospheric pressure CVD), tube position, while other are categorized according to the precursor characteristics to define the reactor type (Metal-Organic, Aerosol Assisted, Direct Liquid Injection CVD), or their Heat Source (Hot Wire, Plasma Enhanced, Thermal).

TCVD, are common setups on semiconductor industry, which allows an easy adjustment of procedures without the implementation of new reactor topologies, increasing the transition costs associated to the introduction of graphene in this industry. Nonetheless, traditional TCVD reactors, which come in a variety of deposition tube shapes and can be operated in low and atmospheric pressure, exhibit a series of advantages and disadvantages to the growth of pristine graphene. In the pro side, the large volume and scalability of the process, as for the con side, the difficulty to achieve large area pristine graphene deposition reproducibility has been already demonstrated. This difficulty can be overcome using longer deposition cycles, lower concentration of carbon source, high purity of the catalytic surface or even encapsulation of the sample in a sarcophagus apparatus, or rapid cooling temperature, enabled by moving the hot furnace from the deposition area.

CWCVD conditions was also largely investigated. The main difference to the TCVD process lies on the heat source. In this case, the hot zone is not the region of the reactor where the sample is placed, but the sample or a region of it. The gases inside the reactor reach the catalytic surface cold, therefore with lower energy, allowing for located depositions, constrained to the hot areas. This statement brings new difficulties, as temperature gradients, and their distribution on a complex geometry sample. Nonetheless its applicability on a roll-to-roll reactor is of great interest when imagining a reactor capable of producing a large area, single crystal graphene with controlled number of layers.

CWCVD shares also disadvantages with TCVD for achieving large area single crystal graphene. This problem arises from the deposition dynamics per se and is not so much linked to heat source shape or distribution.

3. Substrate materials and growth mechanism

Graphene deposition over metallic samples and the carbon source dehydrogenation catalysis is dependent on the sample base material. In this work, Cu pure metal and CuNi alloy were used as catalytic surfaces.

The graphene deposition process mechanism in copper is governed by carbon migration on its surface (Figure I-1). Two stages can be analysed separately at first, the nucleation process where occurs the growth of individual crystal, and their coalescence. During the nucleation process over polycrystalline copper sheets, the isolated carbon adatoms merge together preferably near copper crystal matrix defect sites, as impurities or grain boundaries (GB), where the binding energy of the Cu-C pair is lower. Therefore, the surface crystallographic orientations of the Cu matrix, with different characteristic Cu-C binding energies will have different nucleation rates, and subsequently different graphene etching rates, by the action of hydrogenation, influencing the nucleation preferentiality over the sheet, [1]. The Arrhenius equations for surface and bulk atom diffusion in metals (equations (1) and (2), respectively) help to represent the competing elements on carbon availability for the graphene domains (GrD) growth process.

$$S_T = S_0 \cdot e^{\left(\frac{H_P}{k_B T}\right)} \quad (1)$$

$$D_T = D_0 \cdot e^{\left(-\frac{E_D}{k_B T}\right)} \quad (2)$$

Where S_T and D_T stand for the carbon solubility and diffusivity, respectively, given by the Arrhenius equations, S_0 and D_0 the material specific temperature independent entropic coefficients, H_P the heat of precipitation, E_D the diffusion activation energy, k_B the Boltzmann constant and T the temperature. The specific coefficients values can be consulted in the literature. These two equations balance is dependent on the material of choice and its crystallographic characteristics, which will define the respective activation energies, and the adequate deposition temperature.

The graphene growth process on nickel surface is governed by catalytic dissociation of the hydrocarbon and absorption of the carbon atoms into the bulk sample, which is a function of the sample temperature (Figure I-1) [2]. The same surface dehydrogenation processes take place on its surface, but bulk absorption is preferable over surface migration because of the higher carbon solubility on Ni comparatively to Cu [3]. Graphene nucleation and aggregation takes place during the cooling step, when the carbon atoms segregate to the Ni surface, and surface diffusion becomes dominant, forming graphene (Gr) nucleation zones, which grow individually until coalesce and ideally form a uniform lattice [4], [5].

Other route already explored is to grow graphene over a copper-nickel alloy. Studies revealed that the nickel content on the Cu_xNi_y (with x+y=1) alloy greatly influence the catalytic characteristic of the alloy in the hydrocarbon decomposition, and on the graphene formation [6]. For y<0.1 the graphene growth is mediated by copper type catalysis, due to the diffusion of Ni sites being located mainly close to the alloy surface. The characteristic Ni catalytic behaviour is revealed upon y>0.15, when the Ni distribution starts to be more uniform along the bulk [7].

This process advantage is revealed when the alloying balance allows for a surface mediated catalysis, at the same time it decreases the hydrocarbon dissociation energy to lower values than copper, lowers the surface and bulk diffusion energies for the carbon atom movement, while maintaining copper's crystallographic lattice, which also presents a smaller difference to pristine graphene lattice. Meaning that the graphene deposition is mainly surface mediated at the same time the carbon source is not restricted to direct catalytic products at the surface but also have a bulk source contribution, increasing the available carbon adatoms and consequently the Gr crystal growth speed [8].

The reaction path is influenced by the initial carbon concentration in the metal [4], its crystallographic dominant orientation [9]–[12], defects density [13], temperature at which the reaction is held [12], [14]–[18] and the CH_4, H_2 and Ar relative concentrations. The carbon solubility of the metallic sample influences the available carbon atom dissolved in the sample, or carbon adatom concentration for a certain reaction temperature [19]. This factor can limit graphene growth from lack of available carbon on the nucleation surroundings [20].

Nucleation dominates the beginning of graphene growth whatever the catalytic surface and influences the follow-up aggregation process. To achieve monocrystal Gr along a large area by CVD process, a common practice is to reduce the nucleation sites, which probabilistically will reduce the defects attributed to GB angle differences at the coalescence points [6].

For a surface mediated catalysis, where the carbon solubility is low (Cu metal or low index CuNi alloy [4]), when C adatoms concentration reach a critical saturation point on the catalytic surface, these start to bundle at the lower nucleation activation sites [20]. This is also close linked to impurities present on the surface [13]. Catalytic activation energy of the carbon precursor gas dissociation and C mobility on the catalytic surface are lattice dependent, therefore, nucleation speed is anisotropic along a polycrystalline surface [21].

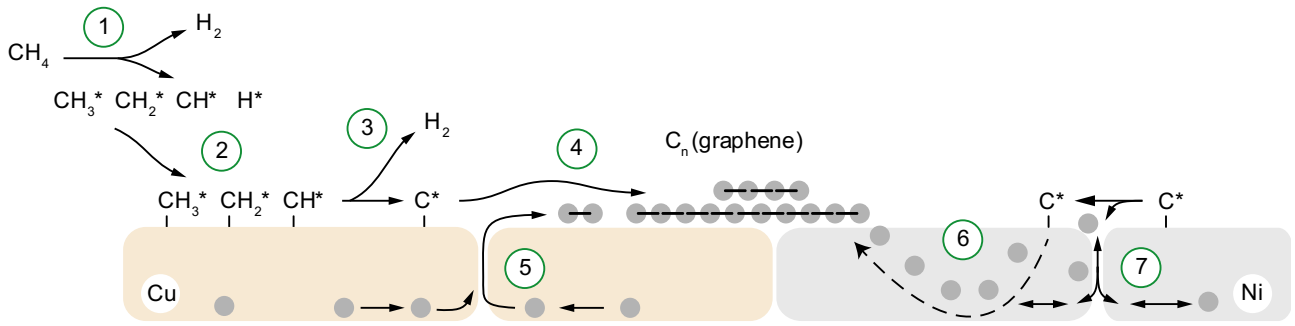

Figure I-1: Schematic diagram of graphene grown over copper and nickel. The processes (1)-(4) are common to both Cu and Ni substrates and the process (5) is a characteristic of the Ni catalytic process, which can be divided by bulk diffusion during high temperatures regimes and carbon segregation to the surface during cooling step. (1) represents the pyrolytic dehydrogenation of methane into carbonions or radicals active species (represented by the superscript *); (2) the metal catalytic assisted dehydrogenation, mediated by the metal type; (3) the isolated carbon radical surface diffusion present on Cu, analog to (6) in Ni; (4) represents the nucleation, Gr crystal growth, crystal aggregation and multilayer formation; (5) represents the dissolved carbon atoms on Cu segregation through the GB; and (7) accounts for the GB carbon adatoms/bulk-dissolved atoms dissolution/segregation on nickel. Adapted from references [21], [22]

On an anisotropic surface, impurities and crystallographic boundaries or steps have lower energy barrier for nucleation than a flat crystal plateau, contributing as a competing inhomogeneity on nucleation distribution along the surface [20]. Surface passivation is one of the routes to reduce this competitive nucleation sites. It is done chemically, using a wet etchant during the initial sample cleaning, to remove impurities from the surface at the same time reduces the native oxide layer [23]. Different wet etchants were already characterized, namely their effect on the catalytic surface, level of surface passivation, reaction time, safety or environmental priorities. Nitric [24] and acetic [25] acids are two etchants largely employed [26], when comparing both, HNO_3 has a higher reduction capability.

Annealing is a standard procedure to increase surface smoothness in polycrystalline metallic samples. This process uses high temperatures to promote atoms movement and crystal growth [27], reducing GB density. Using Cu as an example, during annealing under H_2 flow, the native oxide layer is removed and the Cu(111) grows preferentially [28], in contrast to the case where the annealing is made in the presence of the oxide layer, the preferential orientation is the Cu(001), and the crystal size remains small in comparison to oxide layer free copper surface. This is justified by DFT calculations in [11], where the surface energy of Cu(111)

is pointed out to be 0.15 eV lower that Cu(001); and in the presence of the oxide layer O/Cu(001) gets 0.16 eV lower than O/Cu(111), indicating that (001) crystal orientation is favoured in the presence of the oxide layer and (111) is favoured on its absence. Furthermore, they also show a dependence on annealing temperature and preferential crystallographic orientation evolution, linked to the energy barrier between Cu(001) and Cu(111) to be 0.24 eV. High temperatures are required to preferentially grow the latter.

Apart from the native surface oxide, oxidation clusters remain enclosed in the sample bulk. Their release can affect the growth if it happens during the deposition. Therefore, the annealing duration is an important variable, to guarantee the necessary time of segregation [29], [30]. A technique which has shown improvements at this stage is the intentional oxidation of the sample in the beginning of the annealing process, and after a total sample coverage, its removal by H_2 stream. This contributes to a highest oxygen segregation rate to the surface where it is removed with the rest of the thick oxide layer [31].

Immediately after the nucleation, in conditions of high C concentration in the GrD surroundings, GrD facets evolution are shaped by the C energy of attachment barrier to GrD, which depends on their epitaxial mismatch to the metallic surface lattice orientation, meaning the reaction path can be considered in an interface-attachment-limited regime. Surface smoothness and nucleation sites highly influence this growing phase in the sense that step edges of a rough surface have higher activation energies for C-GrD attachment when compared to C-M, meaning the radial growth velocity can be different for each facet normal, leading to a anisotropic lateral growth and loss of GrD symmetry.

As C source continues to be available, anisotropy of the C attachment process across the GrD expansion directions through different morphological influence sites gets more evidenced. This is governed by the lowest diffusion energy for C adatom and aggregation paths available on the GrD surroundings [32]. This changes the growth to a diffusion-limited characteristic [21]. One visible characteristic of this growth mechanism, is that, influenced by the GB higher C solubility but lower surface mobility, results in a GrD lateral broadening in the direction of the GB, when its facets or apexes approximate and crosses a GB. The increase in lateral growth velocity is linked to the C adatoms higher concentrations near the GB [33].

The last step of the Gr film formation can be considered the coalescence period, when neighbour GrD merge. This transition can be characterized as dissociation-limited [21], since the Gr film coverage also passivates the catalytic surface, lowering the available C adatoms. Therefore, the metal catalytic characteristic has an important role in this growth point, and a major difference can be understood between surface or bulk (or both) mediated catalysis. The latter(s) is able to maintain C supply even during the catalytic surface area depletion [3].

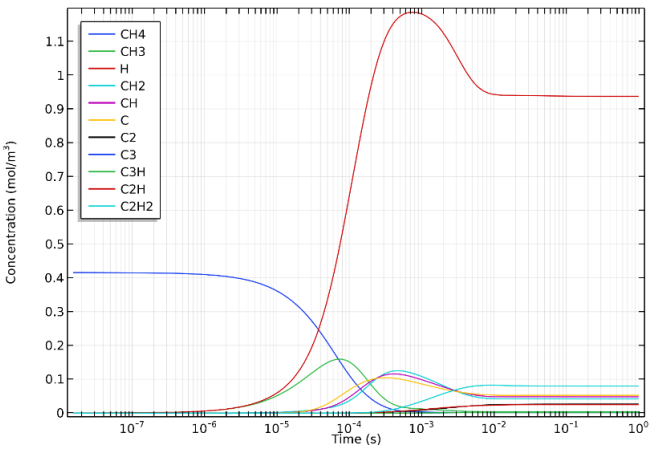

Figure I-2: Carbon species concentrations on the catalytic copper surface during carbon super saturation process, before nucleation. Plotted data from the DFT calculations in article [34].

Hydrogen has a high absorption rate on Ni and Cu [35], which is also dependent on temperature [36], nonetheless its surface concentration is constantly higher than C species (Figure I-2). Through hydrogenation-dehydrogenation reactions on the catalytic surface, H_2 influences the concentration of the participant species and the GrD faced growth kinetics and edges configuration, through the attachment-detachment dynamics of C species [37][11]. Its partial pressure is an important factor for determining the GrD boundaries stabilization characteristic on the catalytic surface [38] and therefore the attachment/detachment energies barriers (EB) of the different C species available, which to become a dominant contributor should have high surface concentration, low attachment and high detachment EB. This indicates that H_2 contribution to GrD etch is a competition between GrD-H stabilization and its contribution for the hydrogenation and surface desorption of detached C containing species, if surface C concentration reduces [34], [39].

4. Temperature

After the nucleation process, growth dynamics are influenced by substrate crystalline orientation. For a given C adatom concentration, diffusion and growth are balanced by their relative energy barriers, which are temperature dependent through equations (1) and (2). Considering this, we can think in terms of the growth/dissolution chemical potential equation [10]:

$$\Delta\mu \approx k_B T \, ln\left(\frac{c}{c_{eq}}\right) \tag{3}$$

where k is the Boltzmann constant, T the temperature in K, c the carbon adatom concentration around the GrD and c_{eq} the equilibrium adatom concentration. Graphene domains grow when $c>c_{eq}$, while a contraction occurs for $c<c_{eq}$ due to C dissolution, along with etching by surface hydrogenation. From equation (3), the C supersaturation model can be considered.

Bulk diffusion is prominent at high temperatures while surface diffusion is preferred at lower temperatures [22]. This can trigger different deposition regimes, which are also strongly dependent on the substrate catalytic nature.

At lower temperatures, in high carbon solubility metals, as Ni, carbon segregation increases, leading to a positive $c>c_{eq}$, while for higher temperatures bulk diffusion energy barrier diminishes [1], inverting the relationship, therefore promoting C dissociation from the GrD.

In a low C solubility metal, as Cu, the surface self-diffusion also increases with temperature, influencing the GrD surface morphology [12][40]. This surface thermal behaviour imposes a biaxial pressure on the Gr layer, inducing it to rotate until it relaxes at the lower energy state possible, relative to the underlying lattice [16]. On the other hand, at lower temperatures (<960ºC), Cu self-diffusion reduces and C adatom mobility is enhanced, contributing to the diffusion-limited GrD growth regime. Late nucleations are other interesting phenomena which can be observed in high temperature conditions, result of bulk carbon atoms segregation through the Cu GBs, consequence of the lower C diffusion energy paths in this areas [33] (Figure I-1).

Therefore, the temperature at which each growth phase is carried out is crucial to achieve good coverage with low defect density on polycrystalline substrates. The summary of the analysed studies indicates that, during the moments immediately after nucleation, the temperature should be kept high enough to promote GrD strain relaxation, leading to better results on their orientation relative to each other, promoting afterwards better crystal alignment during coalescence. Subsequently, after nucleation

and alignment correction, temperature should be reduced to lower Cu self-diffusion and GrD mobility, without affecting C adatom diffusion. Other advantage in lower temperatures is the reduction of the underlying substrate annealing process, which can induce further thermal stresses on the GrD during growth. This way, lower temperature operation reduces defects and operation cost [19].

Considering the above, temperature is a key variable in leveraging the growth thermodynamics and kinetic phenomena which activate the possible diffusion processes described earlier.

5. The present approach

This chapter aims to explore some of the advantages and disadvantages encountered during the state-of-the-art review and introduce the entanglement with the present work.

Starting with the statement "...Virtually every property of the thin film depends on and can be modified by the deposition process and not all processes produce materials with the same properties. Microstructure, surface morphology, tribological, electrical, and optical properties of the thin film are all controlled by the deposition process.", taken from the reference [41], the importance of every aspect possible to control the deposition is crucial.

In the pursue for graphene deposition process evolution to industry standards, Gr growth was already explored in various conditions of pressure [38], substrate nature [21], [42]–[46], precursor [30], [45], [47][48] and heat sources [42], [45], [47], [49]–[51], yielding different results. The identification of the physical processes involved in each one and therefore their control variables is of upmost importance. However, more exploration must still be done to accomplish this goal.

Considering the control of the main variables, temperature plays a crucial role in the reaction, therefore requiring its reading accuracy. For this reason, the CW arrangement was selected to allow the separation of the hot/cold processing gases and stage inside the transparent set-up which enables optical pyrometry. With this reading, PID control of the heating element can be applied to ensure sample temperature accuracy. It is important to notice that this project was carried out with the heavy constraint of adapting the gas management of the existing thermal CVD reactor to the requirements of the here developed setup.

For these reasons, induction heating was the selected setup, since it meets the above-mentioned requirements and adds the additional advantage of allowing high temperature variation slopes, taking advantage of its extremely low thermal inertia when compared to the resistive heating element isolation bricks of the TCVD.

The development of this setup brought several problems to be solved which compose the most of this thesis content. Therefore, regarding the complexity of the task, the following chapter aims to deconstruct the several contributions to the sample heat equation involved and present them through a series of simulations, developed in the COMSOL Multiphysics software. The work starts with the characterization of the magnetic field generated by the Helmholtz configured coils and their coupling with the sample, to understand the expected heat distribution. This is followed by the characterization of the gas flow and sample radiation contributions to the system's heat function.

This chapter continues with the fundamentals for the understanding of the power circuit and its control approach theory. Finally, the dual color pyrometry theory is introduced, since this is a crucial control element with dedicated calibration during the setup assembly, which created the need to build a specific calibration setup.

Following the theoretical basis, the system's electronic circuitry building blocks are explained, along with the explanation of peculiarities and solutions which lead to the construction of the power source, oscillator phase lock loop, inverter, inductive power

stages (or RLC power circuit as it will be called later) and control philosophy applied. Afterwards, the power circuit simulation is presented, which was a basilar tool to understand the optimization steps taken and compare different solution approaches.

The next chapter explains the several practical steps taken for the circuit development and presents the developed pyrometer calibration setup and the thermal imaging which helped to validate the whole setup here proposed.

After the setup design and construction, it was time of finally use it for real graphene deposition. Chapter VI exposes the deposition process followed and the sample preparation procedures as well as the different tested recipes, finishing with the presentation of results, mostly supported by Raman and SEM characterization. Conclusions follow and future work is proposed.

II. Fundamentals

1. Electromagnetic simulation

In this section, the sample heating by electromagnetic induction is investigated using a stationary finite element simulation built using COMSOL Multiphysics software, in accordance with the theory described in [52]. A mandatory criterion for the quasi-static approximation to be valid is that the dimensions of the simulated structure need to be small compared with the wavelength of the electromagnetic fields [53], for the uniform time varying electromagnetic field approximation to be used. This requirement is rightly fulfilled at the working frequency of ~80 kHz, which approximately leads to an oscillating transverse magnetic field wavelength of 3747.4 m, created by the Helmholtz coil circulating electric current.

The COMSOL Multiphysics Magnetic Fields module uses the magnetostatics relationships of the Maxwell equations, equations (1), from where the frequency domain is obtained by Fourier transform, allowing the simulation for the stationary problem with an oscillating electromagnetic field, thus reducing the amount of computation power needed when compared with a full transient solver.

$$\begin{aligned} \nabla \times \boldsymbol{H} &= \boldsymbol{J} \\ \boldsymbol{B} &= \nabla \times \boldsymbol{A} \\ \boldsymbol{J} &= \sigma \boldsymbol{E} \end{aligned} \tag{4}$$

Where H and E are the magnetic and electric fields intensities, respectively, J the current density and A is the magnetic vector potential and B the magnetic flux density.

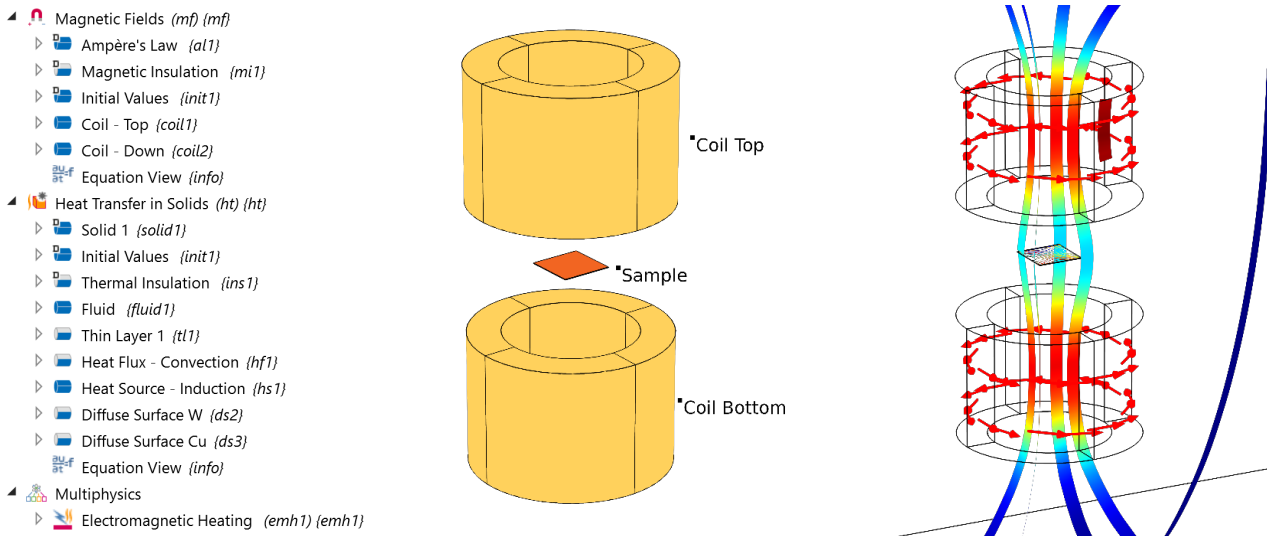

a. b. c.

Figure II-1: a. COMSOL electromagnetic coupled heat transfer simulations function tree; b. simulation 3D cad model of the sample/coils setup; c. simulation result: representations for the circulating currents on the coils, magnetic field distribution and couplig with the sample assembly along with the induced current density distribution on the sample top surface. On Figure II-2.b, the close view of the sample can seen.

This simplified model implemented is composed of two sets of 3 turn copper coils, with a conductor round section of 23.75 mm^2 which accounts for the equivalent conductor transverse cut area of the copper tube used, *coil up*, *coil down*, in a Helmholtz arrangement topology, in which a 167 A@80 kHz current is circulating, as represented by the arrow map in Figure

II-1.c. As it will be seen further, in the experimental setup, this current value is sensibly the double of the real one running through the coil setup. This means that the simulation needs further refinement, although it already supplies good clues to understand the different boundary conditions contributions and their interaction, helping to clarify some observed facts during the deposition process. The sample is composed of a 25 µm thick copper sheet, placed on top of a 500 µm thick tungsten base, intended as a thermal susceptor in the real setup.

When the resulting magnetic field, $\boldsymbol{H_m}$, couples with the sample, it induces Eddy currents $|\boldsymbol{J}|$ fields on the conducting materials. Being copper a diamagnetic material, characterized by its volumetric magnetic susceptibility $\chi_{Cu} = -9.63 \times 10^{-6}$ and tungsten a paramagnetic material, with $\chi_W = 8.84 \times 10^{-5}$, it can be expected that the magnetization field $\boldsymbol{M_{Cu}}$ affecting the copper plate will be smaller and with opposite direction with that in tungsten $\boldsymbol{M_W}$, which will have also the same direction of the magnetic field vector $\boldsymbol{H_m}$, according to:

$$\boldsymbol{M} = \chi_m \boldsymbol{H_m} \tag{5}$$

Consequently, the induced current fields in conducting materials, $\boldsymbol{J_{Cu}}$ and $\boldsymbol{J_W}$ are expected to have also opposite signals with intensities proportional to their resistivities, as described in Figure II-2a. In order to account for this, copper and tungsten resistivities [54][55] were introduced as functions of temperature as boundary conditions (BC).

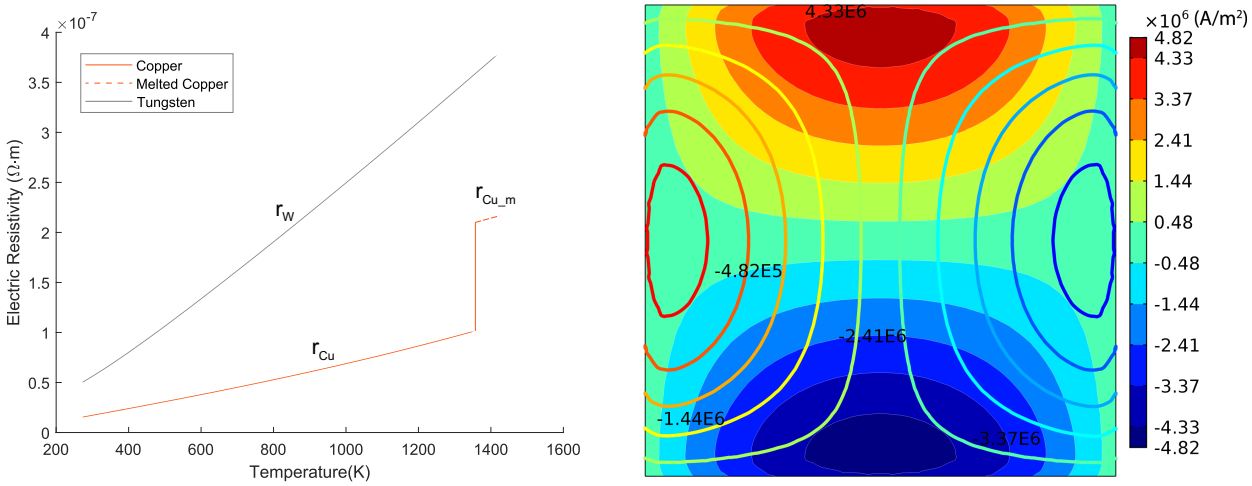

a. b.

Figure II-2: The electrical resistivity as a function of temperature is represented.a for tungsten, copper and molten copper [54][55]. b. induced current density distribution, $\boldsymbol{J_x}$, represented as filled contour, plot under-imposed by $\boldsymbol{J_y}$ plotted as line contour, both in A/m^2.

One of the questions intended to be clarified was the current density distribution along the samples surface area and thickness. The induced Eddy currents have a characteristic depth of penetration along the material thickness, (Figure II-3a) which is dependent on the magnetic field oscillating frequency (f), material intrinsic resistivity (r) and magnetic permeability $(\mu_0\mu_r)$ characteristics:

$$\delta = \sqrt{\frac{2r}{2\pi f \mu_0 \mu_r}} \tag{6}$$

For a conductive material, with isotropic resistivity and magnetic permeability distribution along its volume, the induced current flux depth, δ, is inversely proportional to the frequency which oscillates, allowing to control the heated area depth by only adjusting the frequency. In industry, low frequencies are used in deep heating, whereas for surface hardening, high frequencies are

rather used [56]. In this study, the sample thickness is much thinner than δ, leading to an expected uniform distribution of $\boldsymbol{J}$ along the thickness of copper and tungsten. This is confirmed by the simulation results of $\boldsymbol{J_x}$ and $\boldsymbol{J_y}$ components variation through the sample volume. Figure II-3b plots a line cut along the thickness, $|\boldsymbol{J}|$ maximum intensity zone. $|\boldsymbol{J}|$ is also expected to be proportional to the conductor thickness, meaning the maximum $|\boldsymbol{J}|$ exists for the case where the sample thickness is equal or bigger than δ.

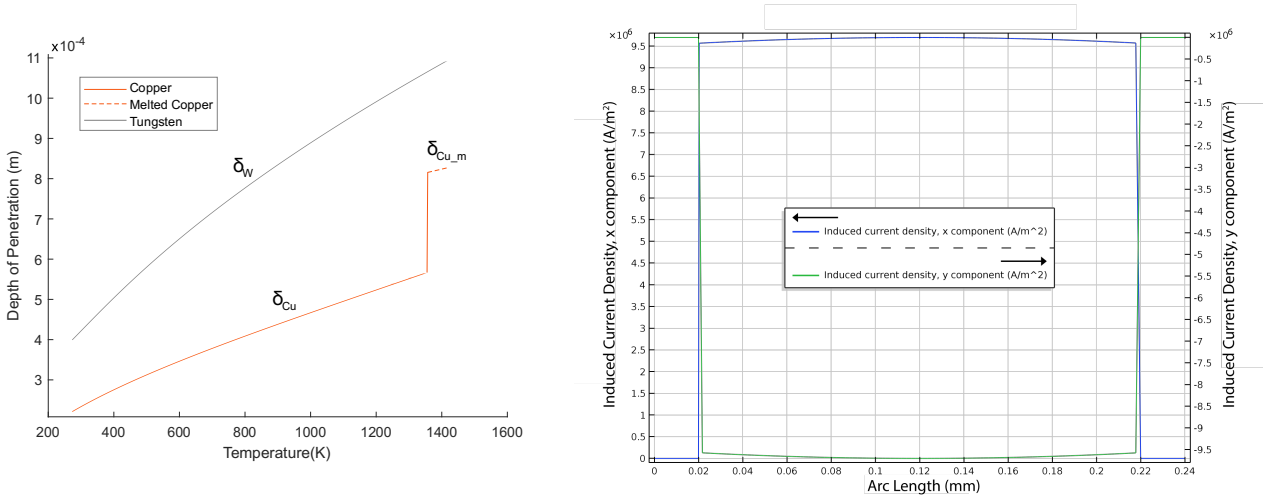

a. b.

Figure II-3.a Eddy current depth (δ) of penetration as a function of temperature for tungsten, copper and molten copper. .b Induced current density, J_x and J_y, distribution, along the sample assembly thickness at their corresponding maximum intensity zones, in A/m^2.

This is an important result, since it allows to consider that the entire sample assembly heats at approximately the same rate, for the selected coil and resonant frequency.

The second part of the simulation uses the Magnetic Fields physics solution with the Heat transfer in Solids interface, coupling both through the Electromagnetic Heating Multiphysics interface [57]. The BC approximate the real reactor environment during deposition as it returns the solution for the conductive and radiative heat transfer function.

$$P = I^2 \cdot R$$
$$Q_{ind} = \frac{P}{V} \tag{7}$$

Where P stands for dissipated power, from ohms law, is equal to the square of the circulating current (I) times the sample resistance (R). The dissipated power per unit of volume (V), yields the heat (Q_{ind}), induced in the conductive material.

The heat source in the sample is provided by Joule heating, corresponding to a power loss that is proportional to the sample resistivity [52]. Figure II-4.b represents the electromagnetic volumetric power loss density distribution throughout the sample, indicating that there is a radial gradient of Q_{ind}, with a maximum near the edges of the square sample. This can be compared with the results shown in Annex 2 for a non-square sample. The results of surface average induced power, calculated from the theoretical approach in reference [52], are plotted in Figure II-4.a and further support the expected dependency of Q_{ind} on the material resistivity and temperature for both copper (solid and liquid) and tungsten during the heating process.

It is important to refer that although the theoretical conditions from the article [52] were simplified, the overall relationship tendency holds for the surface average inducted power variation, with the temperature.

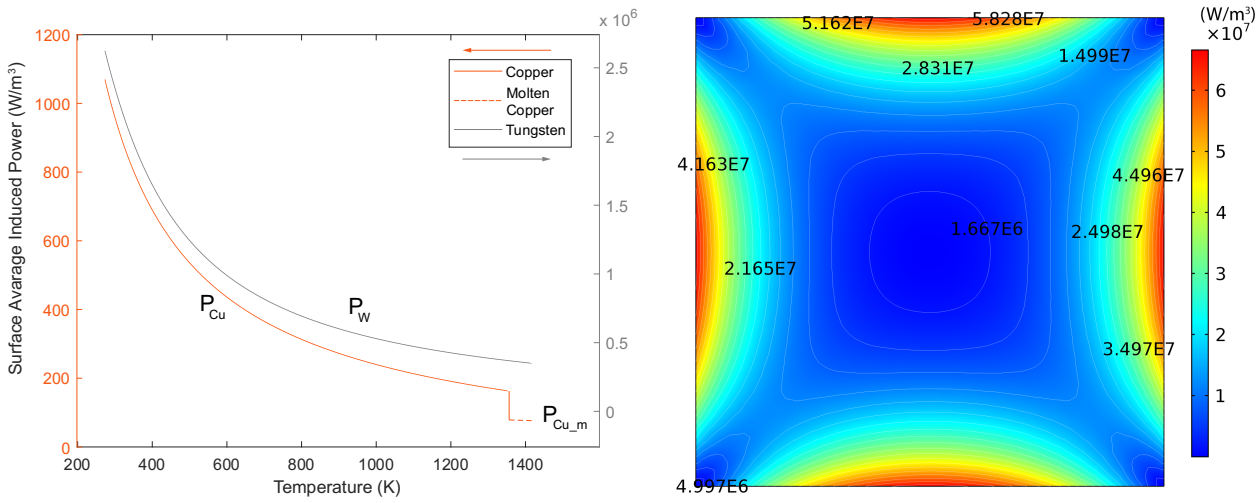

a. b.

Figure II-4.*a* Average surface induced power variation with temperature $Q_{ind}(T)$, evaluated from the theory published in [52], using a magnetic field topology correction factor, g-factor, of -476. .*b* Sample assembly electromagnetic volumetric loss density distribution, evaluated through the COMSOL simulation.

2. System heat function

Inside the sample assembly, heat transfer is governed by heat generation (Figure II-5: a) and conduction, described by equation (8). As seen in the magnetic induction study, heat is generated uniformly along the thickness across the whole volume and its conduction is defined by the heat flux vector $\boldsymbol{q}$, Which is dependent on the materials properties, namely the thermal conductivity coefficient k [58] and the thermal resistivity between the different materials contact pairs [59] describe the heat conduction in a solid, according to Fourier's law of heat conduction.

$$\rho C_p \nabla T + \nabla \cdot \boldsymbol{q} = Q$$
$$\boldsymbol{q} = -k\nabla T \tag{8}$$

Where ρ is the material density, Cp the heat capacity at constant pressure, T the temperature. Q is the heat source, which describes the heat generated by induction on the metallic samples.

From this study, the temperature variation across the copper surface could be clarified. As observed in Figure II-5: b, a gradient of 5 K across the copper volume is observed, with hot spots near the edges, overlapped with the areas where $|\boldsymbol{J}|$ is maximum.

Figure II-5: a describes the temperature variation across the sample thickness in the spot position represented in Figure II-5: b. It shows that the temperature gradient along this direction can be neglected, for this thickness, even though the assembly is composed by different materials. As for the conductive heat flux, the influence of different materials boundary pairs is evidenced by the graphic curvature variation in the arc length position of 0.2 mm and forward [59]. Influenced by the thermal resistivity discontinuities of the contact boundary pairs created by the hexagonal-Boron Nitride (h-BN) layer sprayed in between the tungsten and copper surfaces, to avoid copper diffusion and metal alloying from temperatures above 900°C [60].

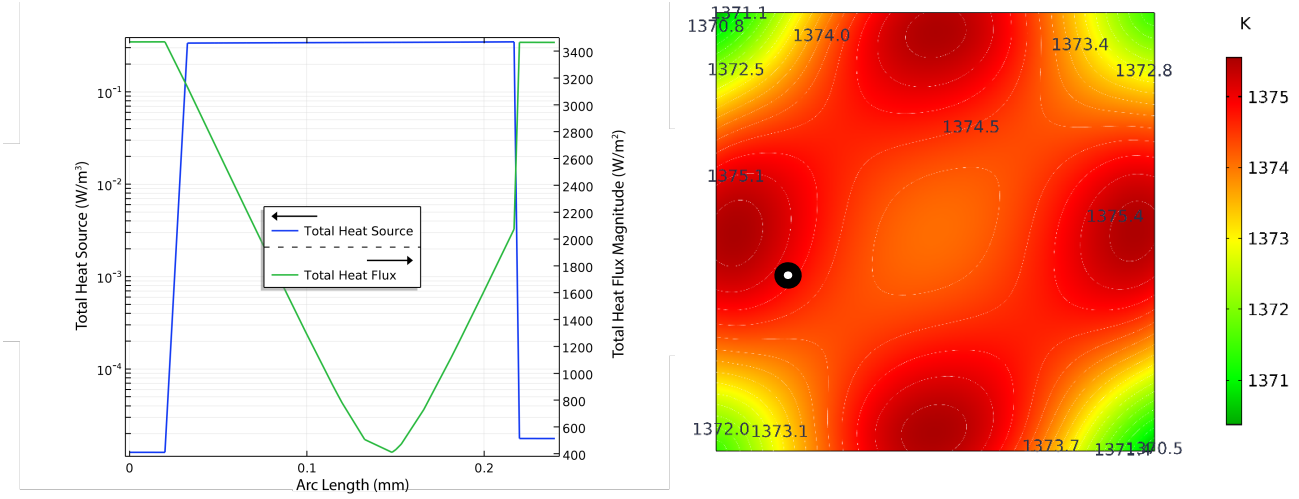

a. b.

Figure II-5: a., sample total heat souce (Q_{ind}) and total heat flux q, ploted along the thickness line in the position pointed on b. which represents temperature distribution in the copper volume

3. Convection

To complete the heat transfer flux characterization inside the Induction Heating CVD (IHCVD) tube, the previously introduced simulation results were fitted in a turbulent flow model, in order to calculate for the convective heat flux contribution, and thus characterizing the temperature distribution surrounding the sample. The effect of temperature on the materials intrinsic properties was considered in the stationary heat equation for the studied temperature, 1080 °C, namely resistivity and emissivity, which influences the total radiative power losses.

The heat distribution function along the tube is governed by convection according to:

$$q_h = h(T_n - T_\infty) \tag{9}$$

where $(T_n - T_\infty)$ represents the difference between the sample and environment temperature, and h is the convective heat transfer coefficient, dependent on the flux boundary conditions [61], [62]:

$$\begin{gathered} h \approx \rho_\infty c_P v_\infty \frac{C_f}{2} \\ v_\infty = \frac{\varphi}{A} \\ C_f = [2\, log_{10}(R_e) - 0{,}65]^{-2{,}3} \\ Re = \frac{v_\infty \cdot d}{\mu}, \mu = \frac{\nu}{\rho} \end{gathered} \tag{10}$$

where v_∞ is the gas flux stray velocity, calculated from the known mass flux inlet, φ. The specific heat coefficient at constant pressure, c_P, is a characteristic of each gas and C_f the skin friction coefficient, describes the flow kinematic viscosity, μ, dependence on the flow cross sectional dimension, d, through the Reynolds number, Re. Furthermore, ν represents the absolute viscosity and ρ_∞ the mixture density.

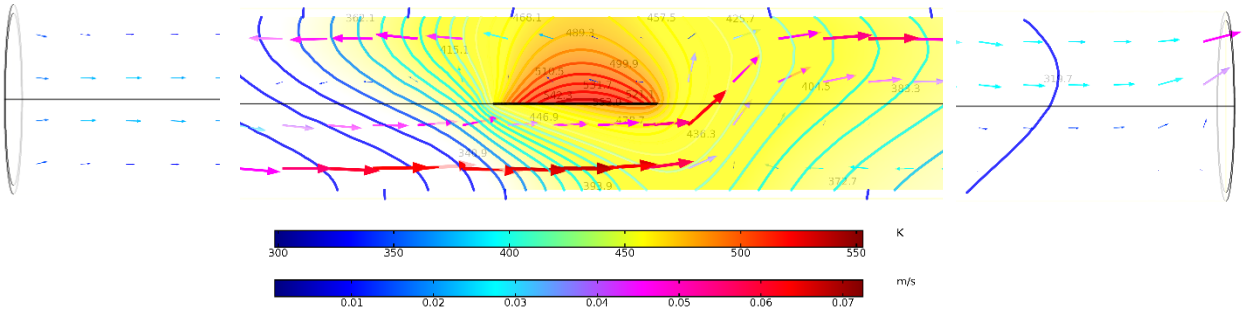

a. b. c.

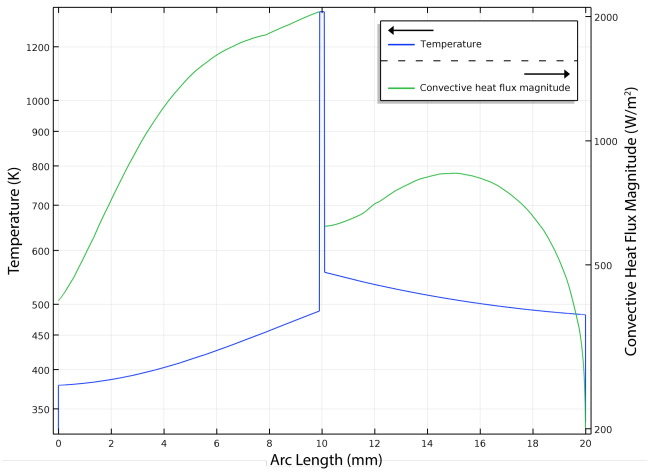

d.

Figure II-6: a. Initial flow simulation inside the 200mm long simulated tube; b. flow and temperature distribution around the sample zone; c. the tube exit considering non back flow boundary condition impose; d. temperature and convective heat flux total magnitude along a normal line passing the sample centre across the reactor tube diameter.

For the present simulation, the gas mixture is composed of xAr, yH_2 and zCH_4 mass flows, with $(x, y, z) = (200, 38, 3)$, so the total mass flow is the sum of the individual gas φ. Since argon is the main component, for all the other variables this gas constants were taken as the mixture constants, for simplicity.

The temperature distribution along the tube diameter, in Figure II-6.d, indicates a temperature gradient of 800 °C between the sample surface and the nearby gas stream, revealing the assumption that with this setup approach, the conditions for the carbon source to dissociate are only catalytic, hence dehydrogenation must occur exclusively on the copper surface. A second conclusion taken from Figure II-6.b is that the temperature in the upper face strongly influences the stream direction, represented by arrows, possibly leading to back circulation of the gas passing above the sample top, caused by convective forces.

This study helps to interpret further the convective heat flux magnitude curve across the sample norm vector of Figure II-6.d. Since $h \propto v_\infty$, from equation(8), as the velocity field diminishes the convective heat transfer follows, which results in a convective heat magnitude difference of more than 0.5 between top and bottom surfaces. Explaining the almost 100 °C temperature difference between these two surfaces, separated by 0.025 mm. According to this result, for practical conditions where just copper is present and no tungsten is needed for the induction heating process, the temperature difference between top and bottom faces can give rise to different Gr deposition mechanisms or even prevent deposition on the bottom face (4-Temperature), depending on the working temperature, even if the gas distribution is isotropic, since the control reference temperature for the system is the

top surface (3-Deposition tube and system assembly). This problem might not be presented in a vertical CVD configuration, since in this case gravity has the same direction of the gas stream.

4. Radiative heat flux

Finally, to account for all the macroscopic contributions to heat transfer in the CVD chamber system, radiative heat flux needs to be understood. Since optical pyrometry was used, as it will be discussed next, the radiative power emitted by the sample surface can be used in order to achieve a better temperature reading control.

Radiative heat flux is proportional to absolute temperature power to the fourth:

$$q_\varepsilon = \varepsilon\sigma(T_s^4 - T_\infty^4) \tag{11}$$

where σ represents the Stefan-Boltzmann constant ($\approx 5{,}67 \times 10^{-8}\ W\ /\ (m^2K^4)$), $(T_s^4 - T_\infty^4)$ the temperature difference between the emitting surface and ambient, while ε stands for the surface emissivity.

The surface emissivity is a proportionality coefficient which relates the specific material radiative flux with the blackbody total radiative flux represented by σ [63]. Therefore, copper and tungsten can be also be treated as grey bodies with specific emissivities as can be seen in Figure II-7.a. Tungsten has a higher emissivity than copper and molten copper, which emissivity also shifts up during phase change. By spectroscopically tracking this associated emissivity shift during phase change, the pyrometer readings could also be calibrated to this critical temperature [64].

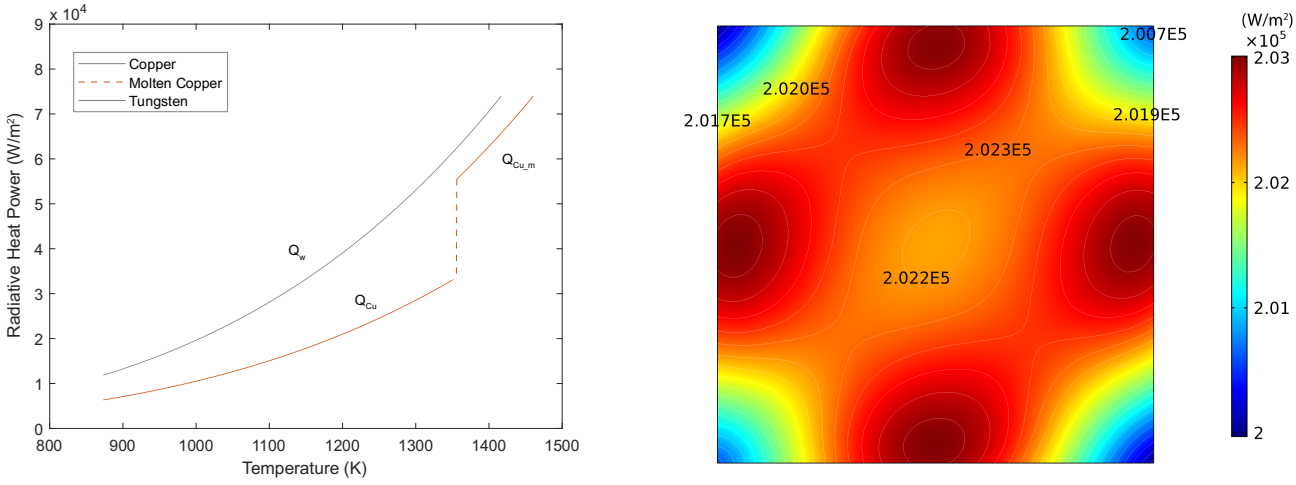

(a) (b)

Figure II-7: a. Radiative heat power as a function of temperature, calculated using the gray body theory for tungsten, copper and molten copper [65], [66], for the sample area; b. Copper surface radiative power distribution.

The radiative heat flux out of the copper surface for the deposition temperature of 1080 °C can be seen in Figure II-7.b, exhibiting a symmetric distribution with symmetry axis along the diagonal, of an approximately uniform radiative flux with a $0.015{\cdot}10^5$ W/m^2 variation between the hottest and coldest places within the sample.

The heat transfer equation for the whole system, needs to include the contributions of the heat sources, conduction, convection and radiative fluxes are summed together to account for the global system contributions:

$$Q_\delta^w + Q_\delta^{Cu} - \left(Q_k^w + Q_k^{Cu} + Q_k^{h-BN}\right) - \left(Q_h^w + Q_h^{Cu}\right) - \left(Q_\varepsilon^w + Q_\varepsilon^{Cu}\right) = 0 \tag{12}$$

where in the superscript indicates the material and the subscript the heat flux type. δ stands for the heat source, occurring just for the metallic materials involved, k is the conductive heat flux, h the convective heat flux and finally ε, the radiative heat transfer function.

The radiative contribution of h-BN is not represented in the equation, since for this study surface to surface radiation was not considered and the h-BN locates in between the copper and tungsten.

5. RLC Series Resonant Circuit

The magnetic field that couples with the sample, heating it by Joule effect through the induced eddy currents, is a result of an electric current circulating in the solenoid L. The following chapter relates the induced heating power calculated in the previous sections with the induction circuit built for this purpose.

The work coil circuit is based on a series RLC topology, composed by a resistive, inductive and capacitive passive elements, Figure II-8, which the output power is modulated by the circulating current oscillation frequency, where the maximum output power is attained at its characteristic resonant frequency f_r.

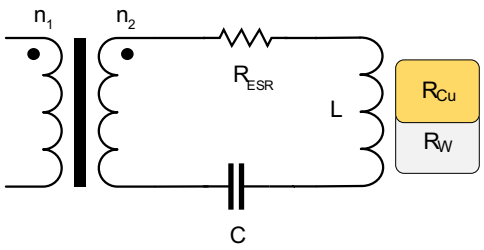

Figure II-8: RLC circuit representation, with internal frequency dependent capacitor resistance R_{ESR}, input ferrite high frequency transformer $(n_1 : n_2) = (18 : 1)$ and external load resistance, represented by the copper and tungsten samples individual resistances.

To better understand, one can ignore any parasitic capacitances or impedances in the circuit and from Kirchhoff laws, write it is the impedance network:

$$|Z_T| = \left(R_T^2 + \left[\omega L - \frac{1}{\omega C} \right]^2 \right)^{1/2} \tag{13}$$

where $|Z_T|$ represents the system's total impedance, L is the heating coil element inductance, C, the capacity of the capacitor tank and R the system total resistance, composed by the capacitor internal resistance [67], the heated samples resistance or loads as they will be called in this chapter. The coil and conductor resistances are ignored, and the total resistance takes the form:

$$R_T = R_{Load} + R_{ESR} = \frac{r_{Cu} \cdot h_{Cu} + r_W \cdot h_W}{A} + R_{ESR} \tag{14}$$

Being R_{ESR} the capacitor internal resistance [67]. Placed inside the coil and contributing to the load resistance (R_{Load}) are the tungsten sample holder, with resistivity r_W and height $h_W = 200\mu m$ and the copper sample, with resistivity r_{Cu} and height $h_{Cu} = 25\mu m$, both sample and holder have the same surface area of $A = 400mm^2$. From this result, and according to Ohms law, the voltage across the resistor (where voltage phase angle, $\phi = \phi_R = 0$) is:

$$|V_R| = \frac{R|V_0|}{|Z_T|} e^{-\mathbb{i}\phi} = \frac{V_0 R_T}{\sqrt{\left({R_T}^2 + \left(\omega L - \frac{1}{\omega C}\right)^2\right)}} \tag{15}$$

It can be seen that $|V_R|$, has its maximum when $\left(\omega L - \frac{1}{\omega C}\right) = 0$ since R_T has a constant characteristic curve which varies with the load temperature, admitting the coil and capacitor are at constant temperature, making:

$$\max|V_R| \implies \omega L - \frac{1}{\omega C} = 0 \implies \omega_0 = \frac{1}{\sqrt{L \cdot C}} \implies f_r = \frac{1}{2\pi\sqrt{L \cdot C}} \tag{16}$$

From this result, we can calculate an approximate value for the resonant frequency and notice that f_r is only dependent of the capacitor, inductor pair.

Since the current over all the circuit must be the same everywhere from the principle of charge conservation, it can be calculated over the resistor:

$$i_0 = \frac{|V_0|}{|Z_T|} e^{-\mathbb{i}\phi} \tag{17}$$

Making the current modulus across the inductor:

$$|i_0| = \frac{V_o}{\sqrt{\left({R_T}^2 + \left(\omega L - \frac{1}{\omega C}\right)^2\right)}} \tag{18}$$

The current phase can also be calculated:

$$\phi = Arc\ tan\left[\frac{\left(\omega L - \frac{1}{\omega C}\right)}{R_T}\right] \tag{19}$$

The nominal power of a RLC circuit in resonance, is dependant only on the current that circulates it and the ohmic impedance, as its characteristic reactance cancels. This, as it can be seen in the Figure II-9, greatly increases the nominal power consumed by the circuit, since the characteristic resistance is very low. Equation (20) indicates just this, as:

$$P_{RMS} = \frac{V_{RMS}^2}{R_T} \tag{20}$$

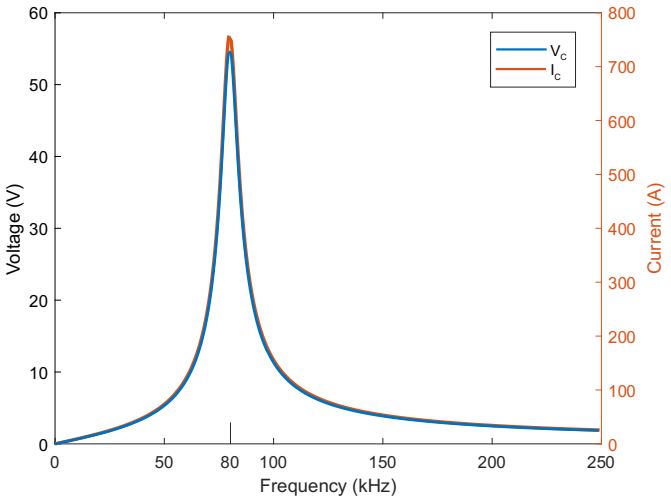

$$f_r = \frac{1}{2\pi\sqrt{L \cdot C}}$$

$$C = 2.6\ \mu F$$

$$L = 1.52\ \mu H$$

$$f_r = 80\ kHz$$

Figure II-9: Resonance frequency peak for the 80kHz ideal resonant RLC circuit.

6. Pyrometry

To measure the copper sample surface temperature through the reactor quartz tube with accuracy and in an electromagnetic induction environment, thermocouple technology cannot be used since its principle lies on measuring the voltage drop through a bi-metal junction and relate the resistance variation with the actual temperature. Since the materials used are metals or alloys, the measurement is directly affected by the induced currents therefore a two color band optical pyrometer (OP)[68] was used for thermometry.

In order to understand the pyrometer operation, we start from the black body irradiated energy spectral distribution (J_{bb}), given by Planks law:

$$J_{bb} = \frac{2hc^2}{\lambda^5} \cdot \frac{1}{e^{\frac{hc}{\lambda k_B T}} - 1} \tag{21}$$

Where, h stands for the Plank's constant in J/s, c for the light velocity in m/s, k_B for the Boltzmann constant in $J \cdot K$. J_{bb} represents the emission spectrum at a determined temperature, so λ stands for the wavelength evaluated in nm and T for the temperature of evaluation in K.

To calculate the irradiated energy spectral distribution of a copper surface (J_{Cu}), the copper surface must be interpret as a graybody, meaning J_{Cu} can be calculated, multiplying J_{bb} by the material characteristic emissivity (ε_{Cu}) [69]:

$$J_{Cu} = \varepsilon_{Cu} \cdot J_{bb} \tag{22}$$

A two colors OP is characterized by its sensitivity to radiation in two spectral bands close to each other , selected by optical filters placed in front of the sensor as it can be seen in Figure II-10.a. This reading mode makes a two-color pyrometer approximately independent of the sample emissivity, if reading bands are sufficiently close to each other any external influence will affect both bands approximately in the same way, with a given error.

It's reading philosophy can be simplified as the resulting slope of the coefficient between the two spectral bands radiative power reading, integrated over the individual band wavelength sensitivity () as can be seen in Figure II-10.b. Ch1 and Ch2 curves represent the band reading over the emitted copper surface spectral power as a function of temperature while Ch1/Ch2 represents the two color pyrometer measurement which can be approximately represented by Figure II-10.b.

$$J_{Cu} = \frac{\int_{0.75\mu m}^{1.1\mu m} \varepsilon_{Cu} \cdot J_{bb}}{\int_{0.95\mu m}^{1.1\mu m} \varepsilon_{Cu} \cdot J_{bb}} = \frac{J_{[0.75\ 1.1]\mu m}}{J_{[0.95\ 1.1]\mu m}} \approx \text{slope} \cdot x + \text{b} \tag{23}$$

Since each pyrometer sensor reads only the radiative power that reach it, $J_{band1,band2}$ must be multiplied by $2A_{Sensor}/A_{Sphere}$ that is the portion of radiation that actually interacts with the sensor (Figure IV-1.b, in the diagram b. point). Results from the sensor area divided by the inverse square law half sphere area, considering only the contribution of the top surface is taken for the reading (Figure II-10). This yields a simple relation of $J_{b1,b2} \cdot r_{sen\_b1,b2}^2/2d_{sph}^2$ between the total emitted radiation and the sensed radiation. Again, a two-color pyrometer neglects this factor if both sensors have the same active area.

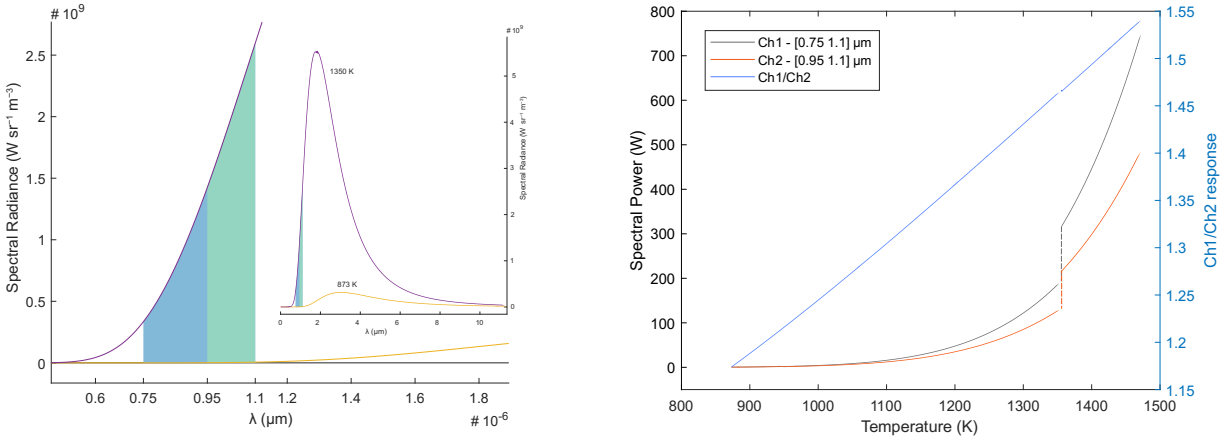

(a) (b)

Figure II-10: a. Pyrometer spectral response bands in blue and green interpolated with the total theoretic spectral radiance for the copper surface for 873K (yellow line) and 1350K (purple line). b. Pyrometer individual channel and two color pyrometer theoretical response for the copper radiance spectrum.

III. Electric and Electronic Circuitry

1. Overview

This section illustrates the circuit set up, detailing some the main components used for the construction of the different circuit stages. Figure III-1 illustrates the link between the different circuit stages, measurement components and reactor tube.

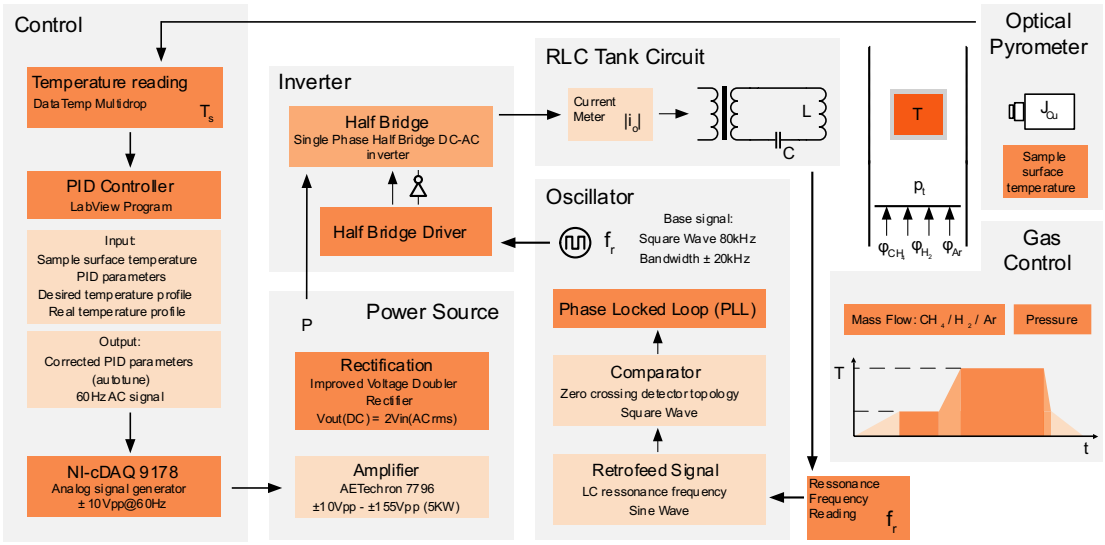

Figure III-1: Heat source complete block scheme, indicating: the control functions; high power components, power source, inverter and RLC tank circuit; dynamic frequency optimization, composed by the phase locked loop (PLL) oscillator block; temperature reading, pyrometer; reactor control variables, tube flow and pressure control.

The induction heating section control variables are the power supplied to the circuit P, the RLC circuit resonant frequency f_r and the sample surface temperature T_s. For the *gas control* section, the control variables are the gas species mass flow φ_{CH_4}, φ_{H_2}, φ_{Ar} and the total pressure inside the reactor tube p_t.

The objective is to inductively heat the copper sample and control T_s to define the proper temperature profile for the graphene deposition process, over the *Cu* surface; for that, a temperature setpoint is given to the *control* program which outputs a 0-10Vrms@60Hz signal through a NI DAQ. This signal feeds the power supply stage that amplifies, rectifies and transmits it to the *inverter* stage; at this point, the signal coming from the *oscillator* is amplified and fed into the *RLC tank circuit*. Here, the coil component couples magnetically with the sample inside it and heats it through joule effect, until the predefined T_s. The surface temperature, read by an optical pyrometer, is used by the *control* program's PID algorithm which adjusts the output signal amplitude. As discussed in chapter 5, *RLC tank circuits* have a characteristic f_r, which is difficult to tune dynamically. For that purpose, the frequency tracking oscillator (PLL) is a crucial part, since it reads the tank current frequency and feeds it to the *inverter* drive, guaranteeing a constant maximum current output, Figure II-9.

The gas *control* side is the existing TCVD control panel which allows for control over the gases mass flows (φ_{CH_4}, φ_{H_2}, φ_{Ar}) and *total pressure* (p_t) inside the reactor. This is achieved by controlling the input mass flows in the inlet pipelines and a proportional valve placed between the reactor exit and the vacuum pump.

2. Oscillator

The oscillator stage plays a central role in the output power optimization, since it dynamically tunes the oscillator frequency f_o with the real RLC circuit frequency f_r. This frequency varies with the sample temperature, or load resistance (R_L), as it is seen in the circuit perspective. Furthermore, a better impedance matching between the power source and RLC circuit is achieved at f_r conditions, as pointed out earlier (II-5). The RLC circuit impedance is ideally real, $Re(Z_t) = R_T$ meaning that its reactance is minimized.

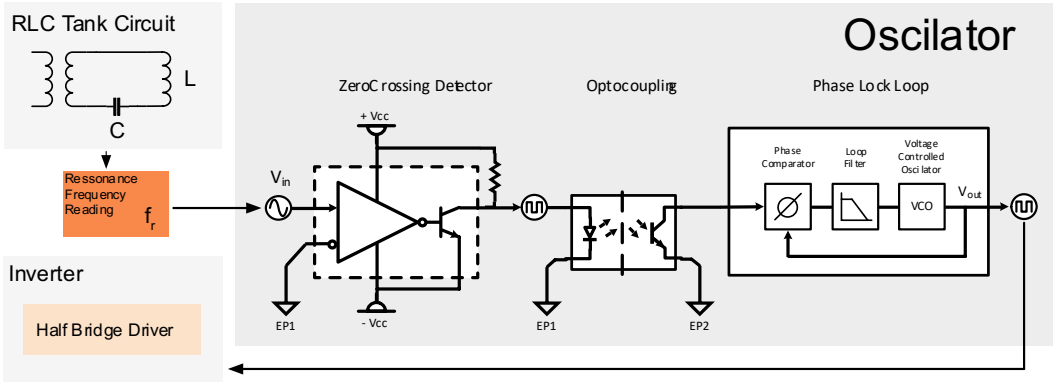

Figure III-2: Oscillator block detail, indicating: the RLC current signal reading block input, and inverter block output; in detail, complies the zero voltage cross detector (ZVS) which transduce the sinusoidal current signal into square pulses; the optocoupling stage, responsible for the signal leveling and isolation; finnaly the phase locked loop (PLL) which compares the current oscillating signal with the incoming one and resizes the voltage controlled oscilator (VCO) output signal to match the input signal frequency.

This oscillator circuit is based on the *CD4046B phase locked loop* (PLL) *integrated circuit* (IC) [70], a *TLP2955* optocoupler IC [71], that serves as decoupler and signal voltage regulator, and a *OPA27* operational amplifier [72] configured as a *Inverting Zero Crossing Detector* (ZVD) configuration.

The general philosophy of this circuit can be followed in the Figure III-2, presupposing the frozen time approach, valid in this application since the time that takes for the conditions to change, and so f_r, is slow compared to the oscillation frequency [73]. The PLL has an internal *Voltage Controlled Oscillator* (VCO) which is set to a frequency close to f_r that defines the decoupled oscillator frequency f_0, and a lock frequency range f_{range}, established as 20kHz through the selection of specific passive components.

When connected to an input square wave signal, frequency f_{in}, the PLL compares its phase ϕ_{in} with its current oscillating frequency phase ϕ_0, and adjust its VCO to output an f_{out} with a phase shift of +90° to the input one, consequently fixing $f_{out} = f_{in}$. This PLL also allows the same operation but with the result to be $\phi_{out} = \phi_{in}$.

Interpreting the RLC resonance condition in the phase space (Figure III-3.a), it is known that the power transfer function to the RLC circuit has a maximum when the inductive and capacitive phasors have the same module, therefore cancel each other ($\phi_L = \phi_C$), reducing the RLC circuit to a purely resistive, where $\Delta\phi = \Delta\phi_R = 0$. From the previous section, this implies that the current $I_{rlc} = i_0$ and voltage across the resistor $V_{rlc} = V_R$ waveforms are in phase:

$$\Delta\phi = \Delta\phi_R = 0 \implies \phi_{rlc}^{Ires} = \phi_{rlc}^{Vres} \tag{24}$$

From the voltage phase variation with frequency in the RLC circuit and in the inverter output, plotted on Figure III-3b, becomes clear the phase relationship between the capacitor (ϕ_{V_C}) and the inverter ($\phi_{V_{in}}$) voltages explored by the PLL to achieve resonance becomes clear. According to the AC analysis, the phase difference between $\phi_{rlc}^{V_C}$ and $\phi_{V_{in}}$ is 90° at f_r, and since the PLL is reading V_C, which phase varies with frequency, and generating V_{in} waveform, which phase is not dependent on frequency, this relation gets fulfilled only for resonant frequency conditions.

The same analysis can be made for the 0° PLL comparison mode, in this case, the target waveform would be the current circulating in the RLC circuit. Again, from Figure III-3b, its AC trace shows that for f_r conditions, it is in phase with the input signal.

Both these measurements are practical to acquire, the difference lies on the redundancy of the method. I_{RLC} waveform can be acquired in any place of the circuit since is equal everywhere, from the charge conservation law. In the present case V_C can just be evaluated between the capacitor poles and its polarity must be considered, since it inverts the acquired signal.

$$\begin{aligned} a\text{:}\quad & f_0 > f_r \;\Rightarrow\; \phi_{rlc}^{V} = \phi_{rlc}^{I} - \Delta\phi_{rlc} \Rightarrow \text{inductive} \\ b\text{:}\quad & f_0 < f_r \;\Rightarrow\; \phi_{rlc}^{V} = \phi_{rlc}^{I} + \Delta\phi_{rlc} \Rightarrow \text{capacitive} \\ c\text{:}\quad & f_0 = f_r \;\Rightarrow\; \phi_{rlc}^{V} = \phi_{rlc}^{I} \Rightarrow \text{resistive, resonant} \\ & \because\; \Delta\phi_{rlc} \in \,]0, \pi[\end{aligned} \tag{25}$$

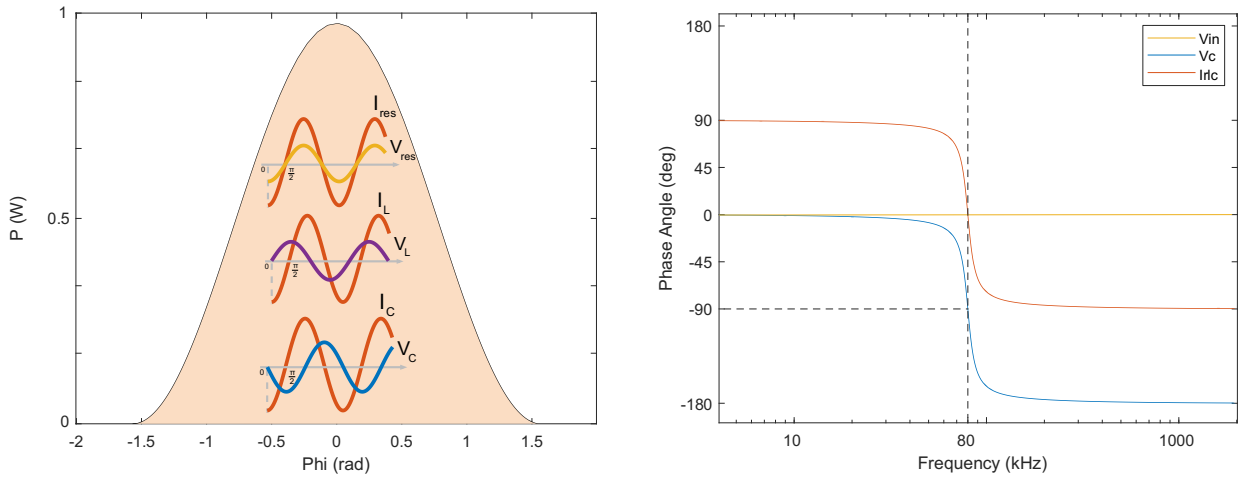

a. b.

Figure III-3: a. Dependence on the power accepted by the RLC circuit with the phase difference between the voltage and current waveforms. b. AC frequency study for the RLC circuit, which reveals the operation of the resonant frequency tuning loop performed by the PLL operation circuit block; simulated using NI Multisim.

The necessary signal conditioning needed to connect the V_{rlc}^{C} signal to the PLL input are handled by the ZVD comparator. The ZVD buffer works comparing its input voltage with a reference voltage and outputs a positive or negative signal, on demand, when the input is above or below this reference voltage.

For this equipment purpose, the input voltage (V_{in}) is compared to ground voltage (V_{gnd}) and the result is a positive signal when $V_{in} > V_{gnd}$ and zero otherwise. From this stage, the signal is just levelled through an optocoupler that accepts a wide range input signal voltage [1 : 20]V and outputs the same signal with a constant maximum of 12V, acting as a signal buffer and isolator, to guarantee the PLL correct work.

3. Inverter

The inverter component is based on a type-D amplifier [74], built with a half-bridge (HB) topology. It amplifies f_{out} signal, generated by the oscillator circuit by pulsing the DC voltage (V_s) supplied by the power source and couples its output, to the RLC circuit, or load, through a toroidal transformer, optimized for medium-high frequencies, by the use of a ferritic core [75]. Figure III-4 represents the schematic blocks of the amplification steps for the circulating signal which take place in the inverter stage.

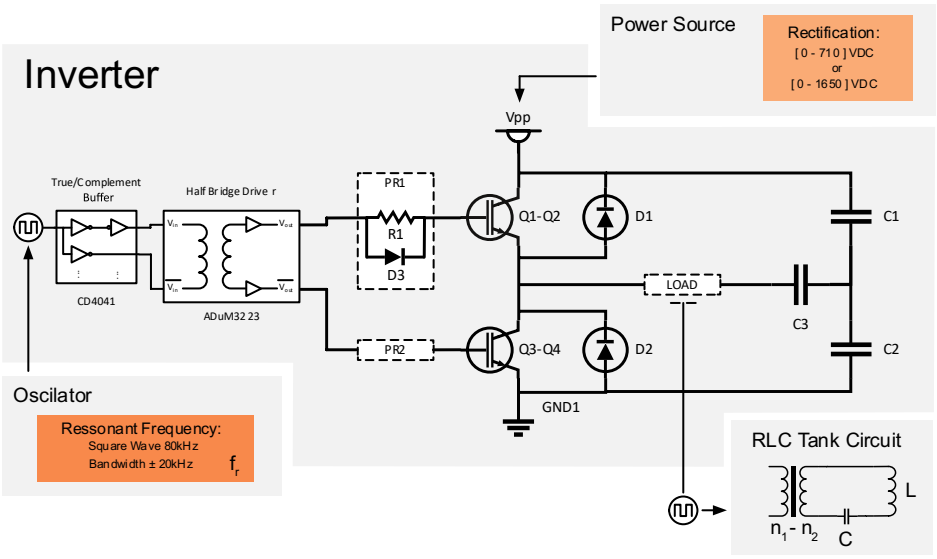

Figure III-4: Inverter detail block, featuring the oscillator and power source input blocks and RLC output block.

The inverter is composed of two parts, the gate driver and the power stage. The gate driver is based on a ADuM3223 IC [76], which provides a galvanic isolated interface between the logic signals coming from the oscillator, and the high power amplifier side. For its operation, the square wave signal generated by the oscillator requires a signal conditioning provided by the *CD4069UB CMOS Hex Inverter* IC [77]. The three used gates provide a buffer and inverter buffer which picks the original oscillator signal and regulates its voltage to 5 Vpp maximum, accepted by the input logic side of the gate driver IC.

The gate driver IC further amplifies the f_r logic signal to drive the HB high and low sides IGBTs devices [78] with a 18 V at 4A signal, referenced to ground for the low side and to the load voltage to the high side. It provides a fast gate charge and enables the smooth operation of the inverter at frequencies between 50 Hz to 250 KHz, which is the maximum locking frequency range provided by the PLL IC configuration. In the current configuration, the maximum operating frequency is rated by the IGBTs maximum rates, fixed by design at 100kHz, easily extendable by exchanging them with high power MOSFETs.

There are two switching elements in the HB as shown in Figure III-4, Q1-Q2 (Sw_1) and Q3-Q4 (Sw_2), each of them composed by two parallel IGBTs to handle higher intensity current intensities. Thinking of them as switches, they are turned on and off in opposite phase, either high side (Q1-Q2) or low side (Q3-Q4), with a duty cycle slightly lower than 50% to prevent high and low sides to be conducting at the same time, resulting in a circuit malfunction.

The capacitor C3 has the important function to mitigate the DC component of the AC inverter waveform passing through the high frequency power transformer, due to normal differences between the high and low side switching elements. C3 Absorbs the DC component an eventual problem of transformer saturation due to flux walking [79].

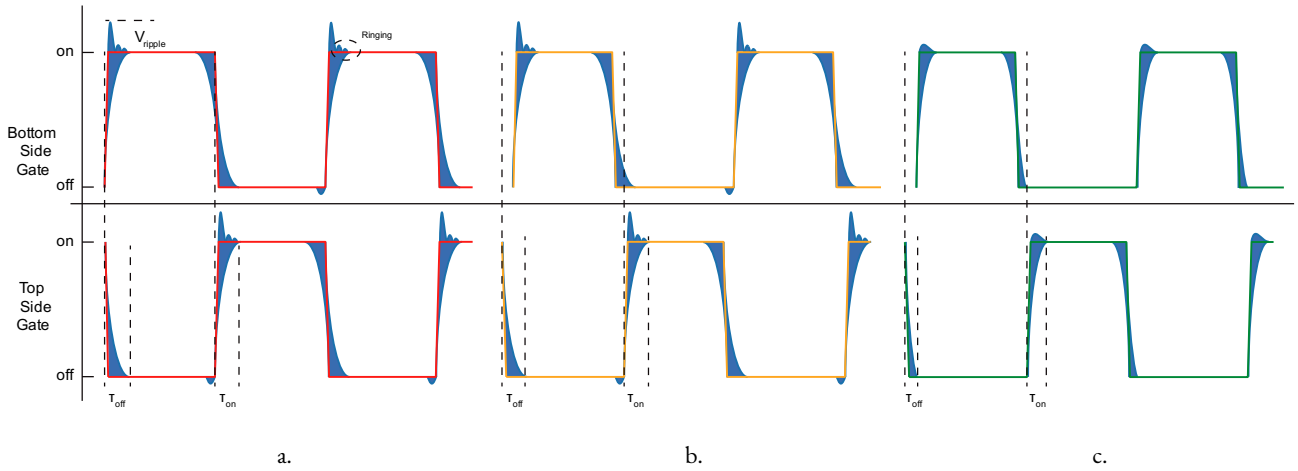

a. b. c.

Figure III-5: Comparison of top and bottom transistor ideal and real gate driving cycle, a. at 50% duty cycle (dC), b. <50% duty cycle and c. <50% duty cycle and adition of gate resistor and diode which compose the PR block seen in Figure III-4.

Gate timing is essential to the correct behaviour of an HB. To avoid catastrophic failure (Figure III-4a and b) the driver takes the input signal, with 50% duty cycle (dC) and models it to a ~45% dC signal to avoid simultaneous opening of the high and low side gates due to a possible delay in the gates open and close time slope. To further mitigate this possible problem, a second level of improvement was implemented before the transistor gates, as the PR stage (Figure III-4).

The PR stage is placed just before the transistor individual gates. This stage is composed by a resistor R_{PR} and a Schottky diode D_{PR}. The resistor, R_{PR}, is required, to prevent oscillations caused by circuit stray inductance and transistor gate capacitance pair, that could lead to an excessive gate-emitter voltage ripple during τ_{on}, at the same time it decouples the parallel transistors from each other. The Schottky diode, D_{PR}, is characterized super-fast recovery time [80] and its very low intrinsic resistance, which serves provides a path for discharging the gate during IGBTs turn off time, creating a node which acts as a RC circuit during the off time step, therefore reducing it by accelerating the gate discharge time, τ_{off}.

The quality factor is a guidance number that shows how the gate driver output responds to a step charge when coupled driving impedance, when inferior than 1 indicates a good component balance for the specific circuit [81]:

$$Q_{tot} = Q_{g1} + Q_{g2} = 2 \cdot \frac{1}{R_{SW} + R_g} \cdot \sqrt{\frac{L_{Trace}}{C_{gs}}} = 2 \cdot \frac{1}{1.1 + 10} \cdot \sqrt{\frac{5\ nH}{2330\ nF}} \approx 0.0082 \qquad (26)$$

Being R_{SW} the internal gate driver resistance, R_g the gate resistance, composed by the internal transistor gate resistance plus R_{PR}, L_{Trace} the PCB stray inductance and C_{gs} the charge needed to open the specific IGBT gate [82]. For this proposed circuit, Q factor is less than 1, indicating a good balance, therefore a good response in on/off transistor time response, enabling this inverter to work in a wide variety of frequencies.

4. Power source

The AC-DC power source stage (Figure III-6) is composed by a passive rectifying stage with added inductances (L1, L2) in the positive and ground of the rectifier, feed by an industrial power amplifier (*PA*) [83], through a step-up transformer. On the output positive side, an exit impedance was also added, to improve the current waveform smoothing during the rectifier handling of high currents [84], creating a LCLC filter [85] on the rectifier output to the inverter.

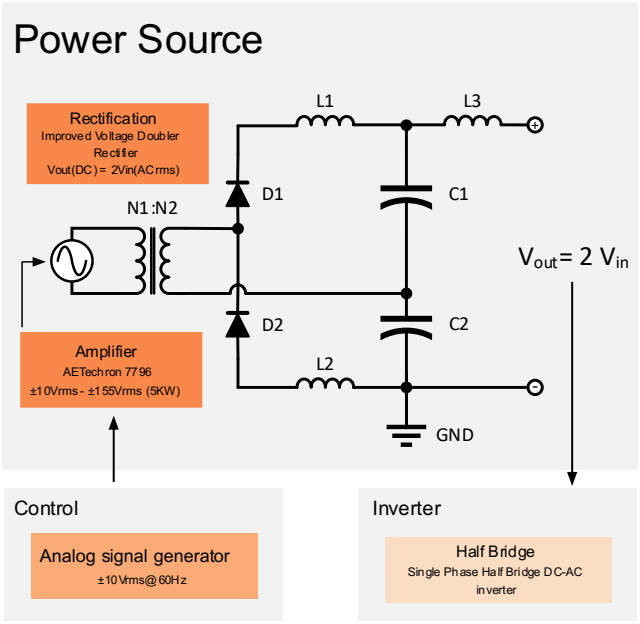

Figure III-6: Power source block composed of a step-up input transformer and a voltage doubler rectifier improved with LC low pass filters on the upper an lower branches; featuring the control input block and inverter output block.

To reduce the energy dissipation due to high currents in the inverter stage, a medium voltage DC power source (0~700 V, 2.5 kW) was assembled. Its topology is based on two superimposed half-wave voltage rectifiers, one rectifying the positive and other the negative half cycle of the input sinusoidal waveform, performing a voltage doubler rectification (VDR), which has the characteristic of outputting twice the voltage sinusoidal waveform, V_{pp} input value, as a rectified DC signal. Pumping charge through a two-stage elevation capacitor bank [86], has the advantage that each capacitor group C1, C2, works at Vin voltage, and not at 2Vin, enabling the usage of lower voltage rated capacitors. Summing on simplicity of implementation it uses only passive elements.

Since the RLC circuit, at resonance frequency, has a nominal power much higher than the power supply can handle due to its low intrinsic resistance (equation (14)), it is expected the current intensity to be high, since it is a voltage supply. To mitigate a possible DC quality factor reduction due to current ripple increase, on top of the normal VDR topology, were added inductors between the diode and capacitor nodes (L1, top, L2, bottom), creating two 2nd order LC filter on each rectification branch, to reduce the DC current ripple. To further stabilize the DC power output at high current demands, another second order LC filter is implemented with L3, using the power inverter capacitors C1, C2 and C3 (see Figure III-4) already implemented on that stage.

The VDR input voltage, Vin, is provided by the output of an step-up transformer (n1:n2=1:3.2) which performs two tasks: multiply the voltage 3.2 times and galvanic isolation of the AC power source from load derived net oscillations, thus giving more safety to the electric system.

Finally, the AC power supply which feeds the input transformer is made of an industrial rated PA [83], [87], set in voltage supply mode, which amplifies the input sinusoidal wave (60 Hz), supplied by the controller output DAQ from 0~10 Vpp to 0~155 Vpp at 5 kW.

Figure III-7 summarizes the voltages and currents measurements taken at the PA and the DC outputs. In open circuit operation (b), the voltage rise is fully developed as expected, showing a linear amplification characteristic of the different circuit elements. When connected to the inverter and its driving load, the high current drained by the RLC circuit limits the voltage on the output

at the DC stage, while the PA output voltage remains unchanged (a). This reveals that the AC power source is isolated from the load as planned.

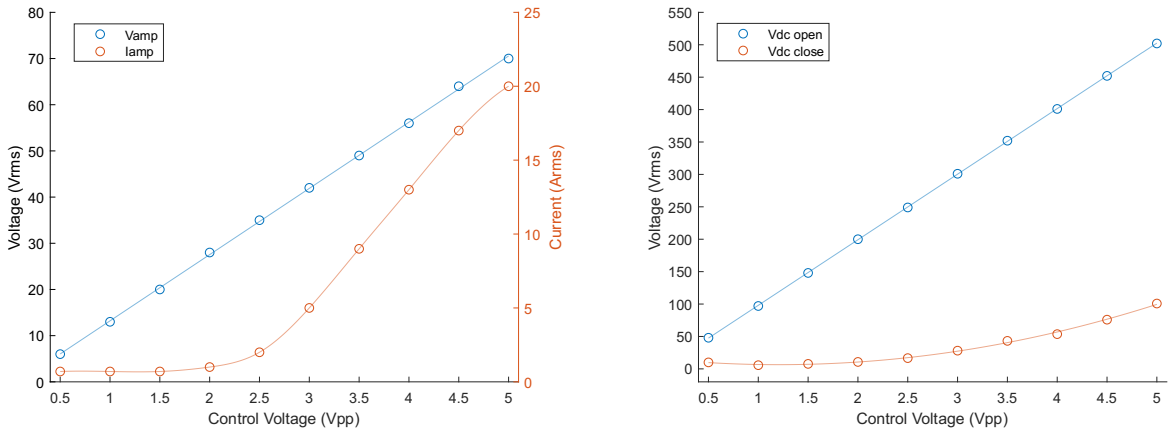

a. b.

Figure III-7: a. Voltage and current profiles on the output of the PA. b. Voltage profile on the output of the VMR, in blue for the open circuit mode and in orange for the circuit work mode, with the RLC coupled load.

It is noticeable in Figure III-7a that until the input voltage passes 1.5 Vpp, the inverter output power is close to zero, increasing in a linear way from that threshold point on. This initial regime can be associated of the inherent circuit losses to the AC/DC converter power source, inverter and RLC circuits.

IV. Equipment Construction and Calibration

1. Circuit construction

The setup is composed by tree independent circuits: (1) an oscillator PLL, (2) inverter half bridge and (3) power source circuits. (1) and (2) were projected and simulated using NI Multisim platform and the PCB layout was performed using Altium 11. The two circuits were then developed tested in a circuit bread board and subsequently built on 3 mm PCB double layer, FR4 dielectric board, using an LPKF E44 CNC for the layers machining and the power pads on (2) were reinforced with 2 mm copper bars. (3) was built using ultrafast diodes in a voltage doubler rectifier configuration, with two 3300 uF rated for 400 V maximum placed in series, at each filter stage, to double the rectifying power stage voltage maximum and two inductances in a LC configuration with the filter capacitors, to provide better behaviour at high currents.

2. Pyrometer calibration

The theoretical development made above is valid as a guide to understand the two-color pyrometer response. Practically, other variables appear, such as the (a) sensor real response which varies with its temperature, (b) the optical focus of the pyrometer lens and (c) the atmospheric gases absorption spectrum difference between both bands. Since the pyrometer reading is a crucial process variable to the experiment control program, its calibration became a main step for the success of this proof of concept.

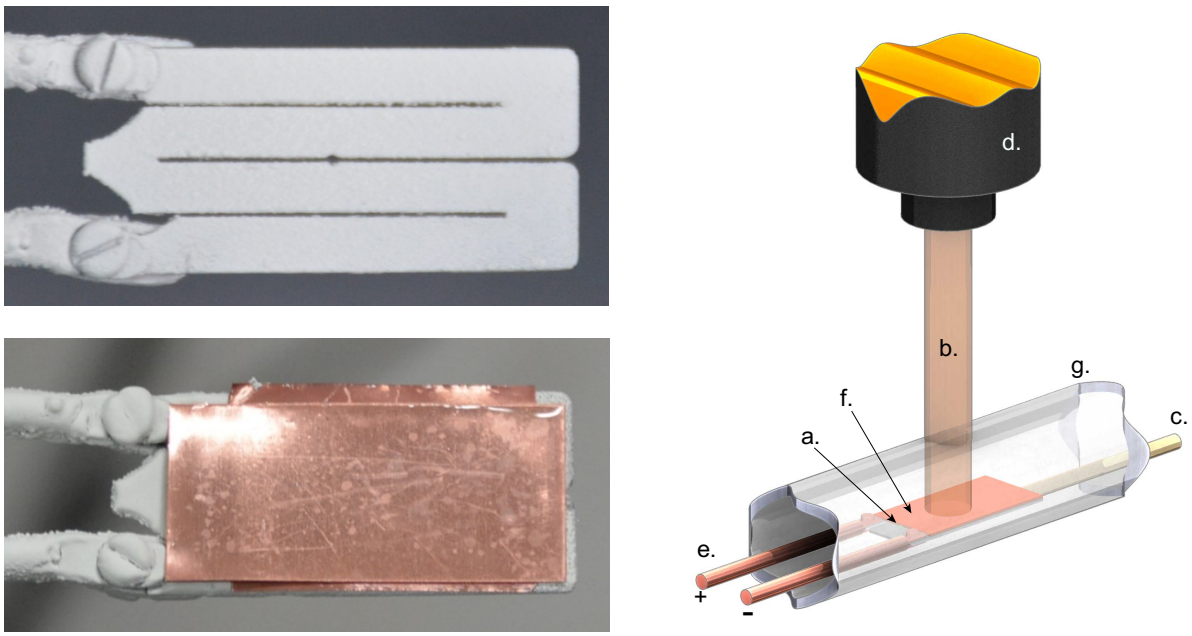

Figure IV-1: Fotographs of the real setup resistance and sample placement, where a 250 µm copper foil was placed on top of a 25 µm to reduce the h-BN radiation contribution to the minimum; Pyrometer calibration setup scheme representing the type-K thermocouple (a.) used to measure the sample temperature and encapsulated in a zirconia tube (c.); the heating element, based on a graphite resistance (e.) coated with h-BN and a power feedthrough; the copper sample (f.) and the pyrometer (d.), placed 500 mm above the sample surface (b.).

To mitigate these sources of error, a calibration setup was assembled (Figure IV-1) using a home-built graphite resistance coated with h-BN spray, to avoid carbon contamination of the copper surface. The calibration setup was placed inside the deposition tube, in a stationary Ar and H_2 (1000:50) atmosphere at a pressure of 280 mBar, after the sample being submitted to the chemical

cleaning procedure. Finally, the pyrometer was placed 500 mm above the sample surface and focused on its centre, a type-K thermocouple was placed in contact with the sample and the external light sources were reduced to the maximum. This setup allowed to compare the thermocouple readings after a temperature stabilization period of 5 min and calibrate the two-color pyrometer slope parameter to fit the unoxidized copper surface specific value of 1.055.

3. Deposition tube and system assembly

The system is assembled in front of the existing TCVD reactor, with the deposition tube, made by a 20 mm diameter 1.5 mm thick wall quartz tube, coupled by KF reducers to its exit in one side and to the vacuum line in the other, with a manual valve in between. The pyrometer is placed ~500 mm directly above the sample surface and focused on its surface, and the coil is placed as represented in Figure IV-2.b, and coupled to a chiller to refrigerate the capacitor/coil pair.

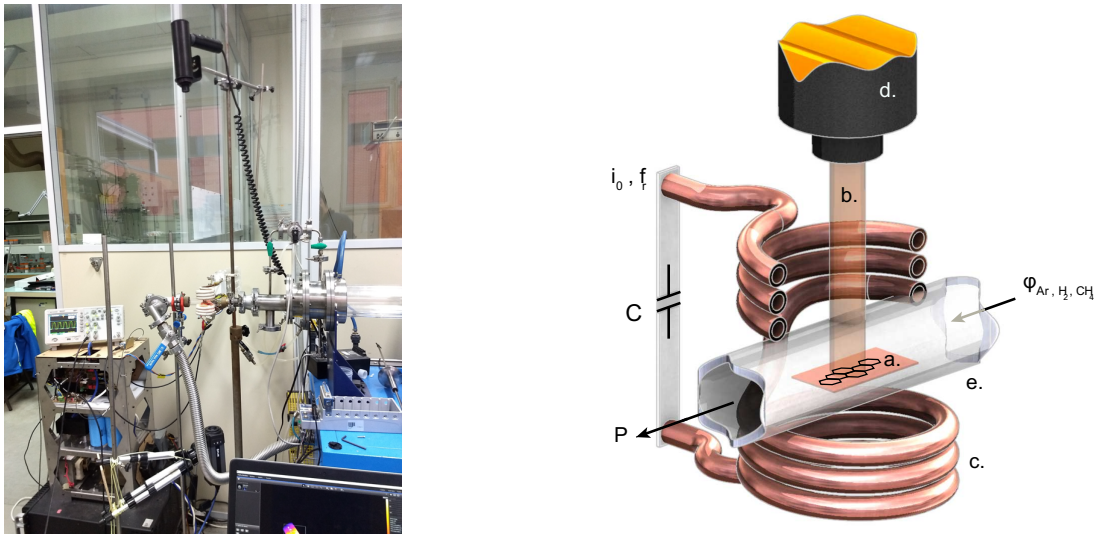

a. b.

Figure IV-2: The setup a., showing the circuitry on the bottom left side, the pyrometer on the top and thermal camera reading from the bottom, the deposition tube attached to the TCVD outlet in one side and to the vacum pump on the other end. b. is a schematic diagram of the setup, showing the different variable involved an discussed until now. Being i_0 the current circulating at a frequency f_r, C, the capacitance the represented circuit variables, while φ stands for the individual gas species involved flux (Ar, argon, H_2, hydrogen and CH_4, for methane gas).

4. Thermal Imaging

Thermal readings were conducted during deposition with a FLIR A310 pyrometric camera [88], with a single band spectral range from 7.5 to 13 μm, which imposes by its pyrometric reading characteristics a dependence on the surface emissivity, which in side view is aggravated by the fact that radiation deriving from copper and tungsten are present. Also, the surrounding environment greatly affect the data collected, leading to a big amount of optical distortion expected on these readings since the sample lies inside the quartz tube, dislocated from its axial plane. Nonetheless the variation in the temperature field across the tube is measurable as indicated in Figure IV-3.a.b. The measurements are taken during deposition conditions and a gradient of 200 ºC that might be over evaluated due to the presence of the quartz tube indicate that methane dissociation energy conditions just exist at a distance of 1 to 2 mm over the copper surface.

Figure IV-3.c plots the relative temperature evolution in five setpoints (SP) during the last steps of deposition. A cooling rate of 32 ºC/s in the sample zone (SP2), 13 ºC/s on the nearby surroundings (SP1, SP3) and rates of 5 ºC/s (SP4, SP5) which indicates

that a good control over the deposition time can be achieved through thermal control of optimum deposition temperature using the advantage of the ability to perform high cooling rates or to control the cooling step as wish.

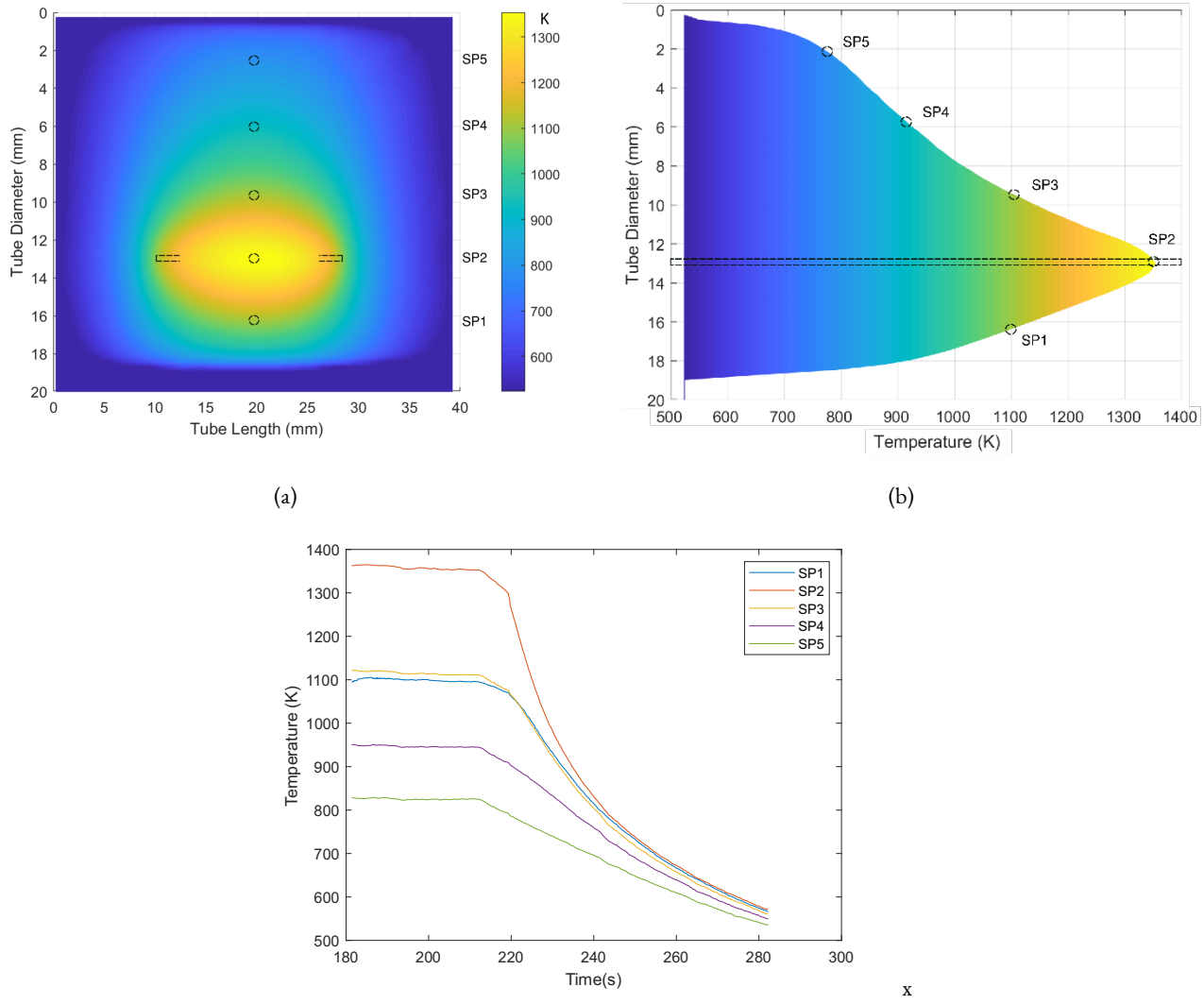

Figure IV-3: a. side view thermal camera shot, indicating the temperature distribution on the deposition area, with b. giving a better spatial understanding of the temperature gradient in relation to the sample assembly position. c. represents the SP1, SP2, SP3, SP4 and SP5 readings during the cooling step of the deposition process.

V. Deposition process

1. Substrate preparation

Graphene was synthesized on polycrystalline Cu foil (25 μm thick Cu-XLP/PHC, purity 99.95 %) using the developed low-pressure IHCVD. The Cu foil substrates were cut into 20 × 20 mm^2 squares and sequentially cleaned by ultrasonication in acetone and isopropanol (15 min each) followed by rinsing in acetic or nitric acid for 30 s. Lastly, the samples were rinsed in isopropanol and left to dry vertically in air. From the two protocols tested, one using acetic acid (60 % in H_2O) and other nitric acid (10 % in H_2O) [89], nitric acid treated samples showed improved copper oxide removal when compared to the acetic acid treated samples. Although this step seemed important for the temperature reading at the beginning, since copper oxides have much higher emissivities than pure copper, which differences could influence the system initialization [90], the native copper oxide did not affect measurably the experiment start and is completely removed in the first annealing step.

After the cleaning and drying process, the sample was mounted on the holder and placed in the higher magnetic field intensity zone. The initialization process was performed manually by increasing the power supply voltage SP until the sample reaches the pyrometer minimum reading temperature, during the primary vacuum stage. This first temperature reading is lower than expected since the pyrometer slope (2-Pyrometer calibration) was calibrated for the pure copper emissivity, whereas the heating initialization process further promotes the sample oxidation, which reacts with the residual air still present in the reactor tube. This process takes around 5 min during which the temperature setpoint is attained and is left to stabilize at 900 °C, while the deposition tube is evacuated until it reaches 0.3 mBar.

After initialization, the annealing step starts when the temperature is adjusted to 1050 °C for the minimum of 5 min and then increased to the final deposition temperature (Table 2). During this step H_2 and Ar gas are introduced in the chamber which is maintained at a constant pressure of Pa = 280 mBar (Table 1). Reacting with the hydrogen present in the gas stream, the copper oxide layer is fully removed [28] [31], which due to the setup layout deposition tube transparency and lack of thermic isolation, can be directly observed. Furthermore, the temperature readings can thereover be trusted after the reduction process takes place. The copper oxide reduction time corresponds to the minimum annealing process time, although graphene deposition rate is dependent on the copper crystal orientation [30][27]. Therefore, for the polycrystalline copper substrate used, the annealing process was stablished to 10 min to allow for crystal reorientation and growth. This step influence on the final graphene film deposition quality is well documented [30]. Nonetheless, for this setup, this was not studied, apart from a group of the samples where the annealing was just 5min as a prof of concept, without however a completely reliable data collection to allow for statistical treatment.

For the deposition step, a series of approaches were tried (Table 2) divided in one-shot deposition (Figure V-1(a), samples 1-6) and a pulsed process (Figure V-1(b), samples 7-10), and some substrate assembly variations, to solve the problem of the EMF (electromagnetic field) power coupling with the copper sample, while maintaining a proper material choice for the graphene deposition [2]. Some observations and thinking lines are explained further in the deposition subchapter. Once annealing is completed, the copper surface is maintained at the deposition temperature in a CH_4, H_2 and Ar flux for a minimum time of 3min, which revealed to be the minimum time needed to achieve graphene nucleation and partial coalescence at the chosen gas concentrations, allowing to observe both processes in the same sample.

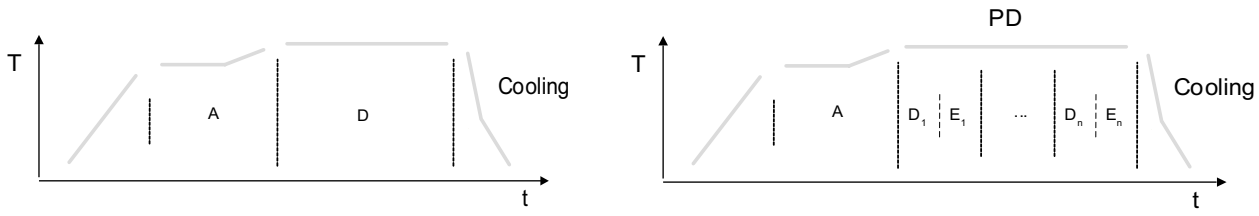

a. samples (1-6); b. samples (7-10)

Figure V-1: CVD recepie guidelines, representing a. one shot deposition and b. pulsed deposition. A, D and E_n stand for Anealing, Deposition and Etch stage acronims, and PD for pulsed deposition.

The pulsed depositions include a reactive, followed by etch step, where the sample is submitted to a variation of H_2 and CH_4 fluxes. Table 2 contains some of the PD recipes studied. Each deposition time step is followed by one minute etch time step, where the carbon source gas is cut and the hydrogen etchant flux is maintained or varied, but always present. During the etch subprocess, temperature and pressure are kept constant.

All samples cooling rate were fast, taking advantage of the setup capabilities in this stage. Fast cooling rates allow to terminate the deposition/etch process abruptly by rapidly returning to the minimum temperature requirements as seen in Figure V-1. In this way, the current graphene deposition is frozen, allowing for an evolutionary study of the graphene growth dependence on the reaction time to be performed accurately, without the need to handle the sample, to remove it from the reactor hot zone.

After the cooling stage, the deposition chamber is evacuated until 1 mBar and then filled with Ar until 500 mBar. For the last step before opening, the air valve is activated until stabilization at atmospheric pressure and then the chamber is open, and the sample removed.

Before the characterization, the sample is placed in a muffle oven for 15 min at 100 °C to promote oxidation of the uncovered Cu sample sites, enabling a first visual characterization.

2. Annealing

Annealing is an important step in graphene deposition on top of crystallographic anisotropic copper surfaces. In this stage, the temperature and gas conditions allow for crystal growth and reorientation [27], [30], surface smoothing, partially mitigating the copper sheet characteristic waviness. Along with that, removal of the native oxide layer and bulk present oxide clusters occur through molecular diffusion of oxygen to the surface [28] and subsequent recombination with the hydrogen radicals present in the flow near the surface. All this improves the surface purity and reduces the roughness, therefore decreasing the deposition variability on copper.

Table 1	Annealing					
Sample number	Duration (min)	Pressure (mbar)	Volumetric Flow Rate (sccm)			Temperature (°C)
			H_2	CH_4	Ar	+
1,2,6-10	10	280	190	0	200	1000 – Dep. T
3,4,5	5	280	190	0	200	1000 – Dep. T

+ - The annealing final temperature is the same as the deposition temperature, as explained in the deposition process above.

For this thesis, a systematic study around the annealing process was not performed, and the only observable which placed a minimum time constraint on this step was the oxide surface layer removal, which was directly observed, as previously explained.

Table 1 summarizes the annealing step procedure, where H_2 acts as the etchant and Ar the carrier gas.

3. Deposition

As stated before on the deposition process description, two methodologies were explored. The one-shot deposition served for the initial exploration of the conditions needed to achieve controlled CVD graphene nucleation and growth. In this initial stage the substrate holder assembly was also considered as a variable since to achieve the deposition temperature and stability a thermal diffusor had to be added due to the low resistivity of copper (Figure II-2(a)). A tungsten (W) plate was the material chosen due to its resistivity, good thermal conductivity and high stability at the operation temperatures. Nonetheless the fact that Cu diffuses to the W crystal matrix at temperatures above 1000°C [60] imposed a new problem of sample removal. Graphene growth was not affected since the bond was just superficial and confined to the W-Cu contact interface.

Table 2	Deposition						
Sample number	Duration (min)	Pressure (mbar)	Volumetric Flow Rate (sccm)			Temperature (°C)	Substrate arrangement
			H_2	CH_4	Ar		*
1	3	280	50	6	200	1050 (1)	W-Ni-Cu (c)
2	3	280	20	6	200	1050 (1)	W-Ni-Cu (c)
3	3	280	50	5	200	1075 (1)	W-Cu (c)
4	3.5	280	50	5	200	1075 (1)	W-Cu (c)
5	4	280	50	5	200	1075 (1)	W-Cu (c)
6	3	280	40	5	200	1025 (1)	W-Cu (p)
7	1+1+1	280	45	5-0	200	1070 (2)	W-HBN-Cu (p)
8	1+1+3	280	45-20	5-0	200	1070 (2)	W-HBN-Cu (p)
9	1+1+1+1	280	45-20	5-0	200	1070 (2)	W-HBN-Cu (p)
10	1+1+1+1	280	45-20	4.5-0	200	1070 (2)	W-HBN-Cu (p)

(1) - Indicates that the temperature was read with the pyrometer in single color mode during the early development, therefore this reading accuracy is low and must not be taken in for comparison.

(2) - Indicates that the temperature was read with the pyrometer calibrated in the two color mode and referred to the fringe apearance temperature, therefore it can be taken for comparison.

* - The substrate arrangement is read from the bottom layer to the top layer, from left to right respectively; the W and Ni layers are 200 µm thick, the Cu layer is 25 µm thick and HBN (or h-BN) spray layer thikness was not measured but did not exceed a few tens of microns.

c – Stands for concave arrangement of the top substrate layer (for all the cases, the Cu precursor layer).

p – Stands for flat arrangement of the top substrate layer (for all the cases, the Cu precursor layer).

This problem opened the opportunity for experimentation, and for samples 1-2 a 200 µm thick nickel (Ni) plate was introduced as a division layer between Cu and W, for two reasons. The first one was to mitigate the W-Cu pair diffusion problem, since Ni minimum diffusion temperature on W is 1350 K [91]. The second reason, linked to the graphene growth procedure, was the

experimentation around the introduction of a carbon absorber metal (Ni) in the chamber. As expected, from the binary phase diagram of Cu-Ni [92], diffusion from the Ni substrate to the Cu sample was observed. The diffusion threshold of Ni on a Cu sample is rated to 19.9% [7] and since the Ni/Cu ratio was ~ 8 in the sample assembly, it is assumed that a good uniformity of the Ni atom distribution on the Cu sample was achieved. Unfortunately, EDS results performed on these samples were not clear about the percentage of nickel. Therefore, the deposition process could not be considered to have just a catalytic surface behaviour for the dehydrogenation reaction of the carbon source seen in a pure copper surface, nor a pure carbon bulk absorption and segregation on cooling, typical of the graphene growth mechanism on Ni substrates. Indeed, in the sample variable side, according to the literature, a mix reaction occurs, which depends intrinsically on the Ni diffusion percentage on the Cu bulk matrix [6]. The regime therefore takes advantage of the high carbon solubility on Ni to compensate for the reduction of available Cu catalytic surface along the graphene deposition time, as graphene clusters gradually occupy and passivate.

In the deposition batches 3-6, graphene was grown in Cu samples, placed on top of a W plate susceptor. These samples suffer from the copper diffusion problem introduced earlier, most visibly in samples 3-5 where the process temperatures were kept high and closer to the Cu melting temperature. In order to mitigate this problem, the Cu samples were arranged on top of the W plate in a concave geometry reducing the contact surface Cu/W pair to the longitudinal edges, promoting at the same time a tunnel formed in the direction of the gas flow. In sample 6, a planar Cu/W contact pair was tested, and the temperature was lowered. Consequently, the sample removal was still possible despite some diffusion occurred, but the final heat dissipator/sample pair did not behave adequately.

The last procedure tests were undertaken with a sample arrangement constituted by a W plate susceptor spray coated with h-BN [93] underneath the Cu sheet substrate. This assembly took advantage of the easy application of the h-BN spray that leaves an uniform, highly refractory and moderate heat conductive coating, providing a diffusion barrier and thus solving the Cu-W problem without introducing a contaminant nor affecting the graphene deposition reactions taking place inside the CVD tube [94]. The h-BN thermal insulating properties did not show measurable consequences in the heat transfer from W to the Cu plate, when evaluating the power drained by the circuit. Lastly, since h-BN creates a coating on top of the W plate, the copper samples were prone to be removed effortlessly and without any damage to the copper/graphene deposition result.

For all the depositions, both the Ar flow and the total pressure inside the chamber were kept constant, while H_2 and the carbon source CH_4 flows were introduced as variables with the deposition time (t). For the first six samples, a total sample coverage was attained. Here, the deposition uniformity and sample assembly stability were the main tests, while for the pulsed deposition (PD) samples, the main objective was to achieve nucleation and partial graphene crystal coalescence to study the effect of evolutionary deposition [95] for the present case. Theoretically, during the first deposition stage, nucleation should be achieved and during the first etch stage hydrogen should remove the nucleation sites associated with lower C-Cu pair dissociation energy and weakly bound carbon layers or secondary nucleation. Then, in the following deposition stage [37], the growth at the preferential nucleation sites should be promoted at higher growth rates. In order to yield good results in this process, both the deposition and etch stages conditions are important since at the n^{th} PD stage, ideally, the preferential nucleation sites should continue to grow, crossing over the Cu GB, and any new nucleation should be etched. Since graphene deposition on Cu is affected by the local crystalline orientation, this technique intents to mitigate this influence by nucleating at the preferential sites and grow the crystal beyond its initial nucleation GB, promoting graphene overgrowth instead of nucleation.

VI. Graphene Characterization

By placing the samples on a oven, after deposition, during 10min, a thin copper oxide layer is readily formed on the non-covered sites of the sample surface, increasing the GrD contrast in comparison to the substrate. All the as grown samples where submitted to this procedure before visually inspection through an optical microscope being carried out. This technique allows for fast post-processing initial characterization and was used to qualitatively evaluate the nucleation density and coverage during the pursue of the nucleation minimum time. The nucleation conditions were achieved for deposition periods under 2 min. A total surface coverage was achieved for depositions over 4 min in continuous mode, indicating that the period that mediates from carbon saturation to full graphene coverage is relatively short.

Figure VI-1.a is an example of the partially covered sample number 7 (Table 2), where different nucleation moments are evident. Shows a relatively high nucleation density, especially nonuniform distribution in the optical field view, being clear different GrD nucleation sizes where coalescence has occurred (right side). The different nucleation sizes can be attributed to different nucleation times, in the pulsed recipe. Smaller nucleations density seems to increase close to copper GB possibly influenced by dissolved C segregation through the closer GB.

For the same sample, Figure VI-1.b shows an interesting deposition phenomenon occurred in the vicinity of the Lichtenberg pattern cuts (see annexes), which occurs due to dielectric break down of the metallic sample under high currents. Near these patterns, Cu was observed to steadily evaporate at low rates, during the deposition and etch periods. The conditions in these areas seemed to favour the deposition of graphene/Cu precipitate, judging by the Raman results which indicate high defective, multilayer graphene.

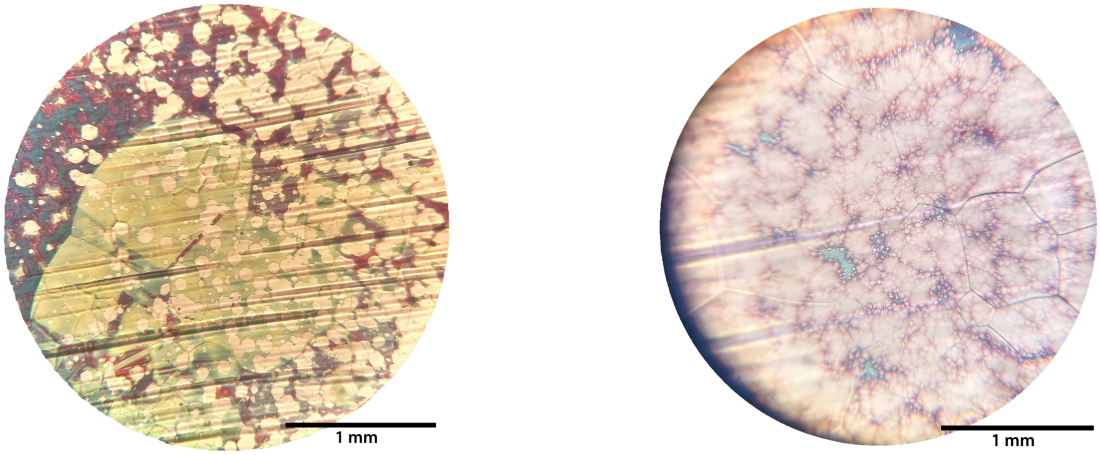

a. b.

Figure VI-1: Optical microscopy fotografies accuired from sample 7 showing (a.) multiple phase nucleation and coalescence zones and (b.) percipitate like deposition observed neer the lishtenberg pattern cuts.

Micro Raman spectroscopy was the technique of choice for rapid characterization of the deposited graphene material. This was accomplished by using a Horiba HR800 instrument assisted by a 442 nm line from a Kimmon He:Cd laser. From Raman spectra, the main vibrational modes of the pristine graphene crystalline lattice can be promptly identified: the D band (~1370 cm^{-1}), the G band (1580 cm^{-1}) and the 2D band (~2686 cm^{-1}, an overtone of the D band) [96]. The activation of the D band is associated with lattice defects [97], while the 2D/G intensity ratio, the G and 2D FWHM and their spectral positions are highly informative of the overall quality, stress state, interaction with the substrate and the number of layers. Raman mapping is also possible in

this equipment and helps to understand the deposition dynamics by providing images that may be superimposed to optical and SEM micrographs, helping to establish a relationship between the local morphology and the crystalline nature of the graphene deposits.

The different recipes lead to a multitude of results. Raman spectroscopy revealed that all the samples have various types of graphene deposited. A comparative plot can be seen in Figure VI-2, were (a.) combines hand chosen examples of single, double and multi-layer graphene, with and without defects. The other plots, (b.), (c.) and (d.), combined form a simple observation of the Gr layer uniformity. From (b.), almost all the samples chosen, present a diversity of Gr layers, indicated by the 2D/G ratio. Also, with a variability of the, defect activated, D band contribution, indicated by the D/G>0 ratio.

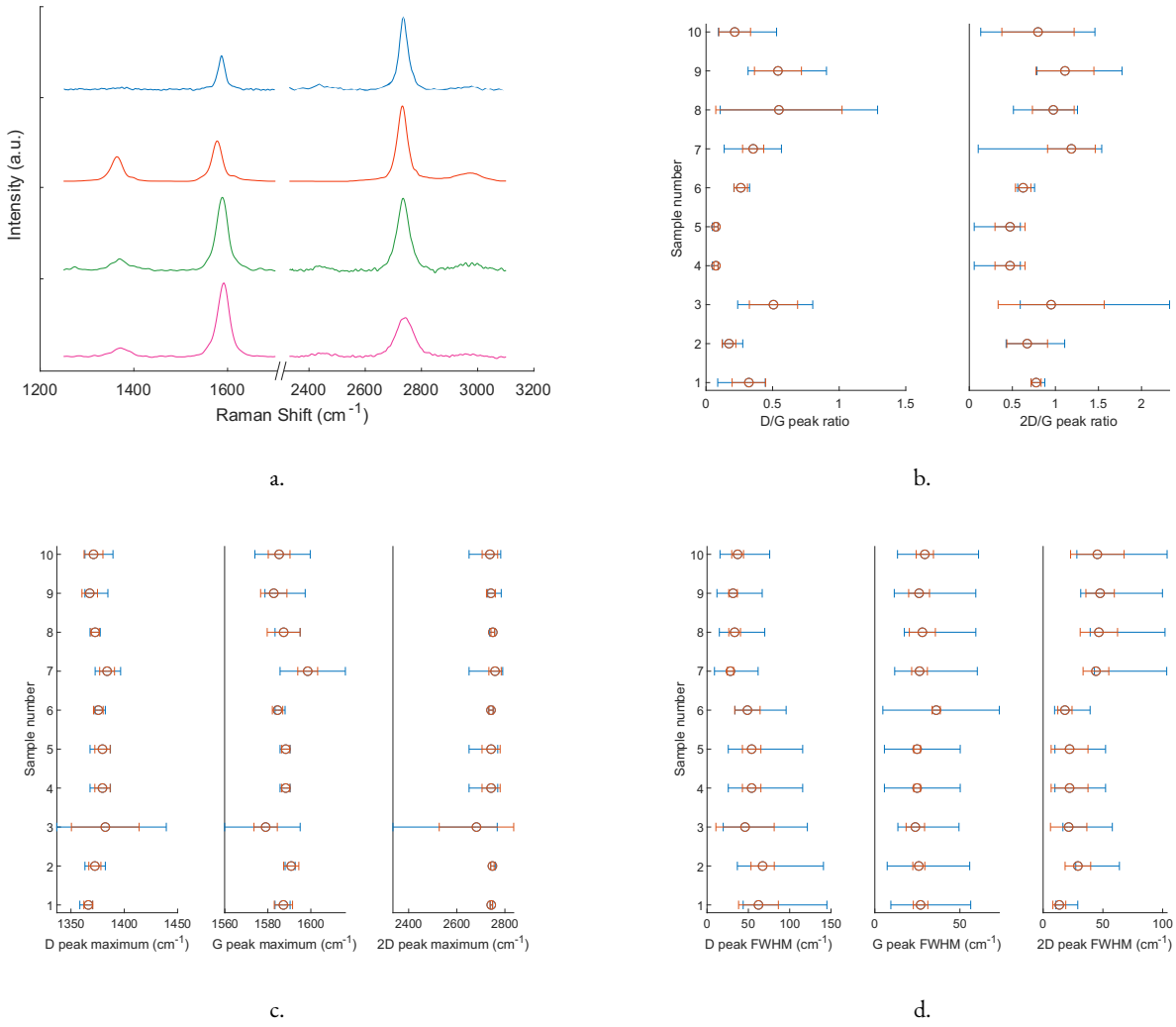

a. b. c. d.

Figure VI-2 Multi spot Raman spectrum (RS) compilatory analysis for each sample. The orange errorbar represents the standart deviation of the data and the blue errorbar represents the maximum and minimum deviations for a specific sample data. Examples of different observed Gr types spectra are represented in (a.), in blue a tipical Single Layer Graphene (SLG) RS, in orange, a SLG with defects associated to the edge type; in green, a bilayer Gr example and in magenta, a multilayer graphene, both with relactive low D band manifestation, activated in this case by lattice the defects on the uniformly covered area.

Gr single layer areas were spotted in sample 3, revealed by the 2D/G ratio >2, but also presented bilayer (1>2D/G>2) and multilayer zones (2D/G<1). This sample also present the biggest diversity of D, G and 2D peak centre and FWHM deviations (from figures c. and d.), which sum together indicate a highly anisotropic graphene coverage, with various deposition states present.

This was attributed to the temperature gradient along the sample surface, consequence of its concave arrangement, leading to temperature influenced product variations.

SEM imaging was also available and was used to give insights of nucleation areas and GrD coalescence. It was performed in sample 7 and 8, Figure VI-3.a. and Figure VI-3.b-d., respectively, which showed a good graphene coverage in the sample centre and a high nucleation density on their limits. Figure VI-3.a. and c. capture the result of pulsed depositions, with the presence multiple GrD sizes, attributed to different nucleation times but a good overall GrD orientation, independently even over different Cu crystal lattices. Figure VI-3.b. and d. are close ups of nucleation sites. (b.) reveals a coalescence defect, revealed by the underlying Cu oxidation promoted after the deposition to enhance GrD contrast, which can be attributed by incomplete coalescence. A close-up of a defect less SLG domain coalescence between GrDs nucleated in different Cu lattice orientations can be spotted, along with hexagonal GrD characteristic of high temperature, low pressure, deposition conditions over Cu catalytic surface

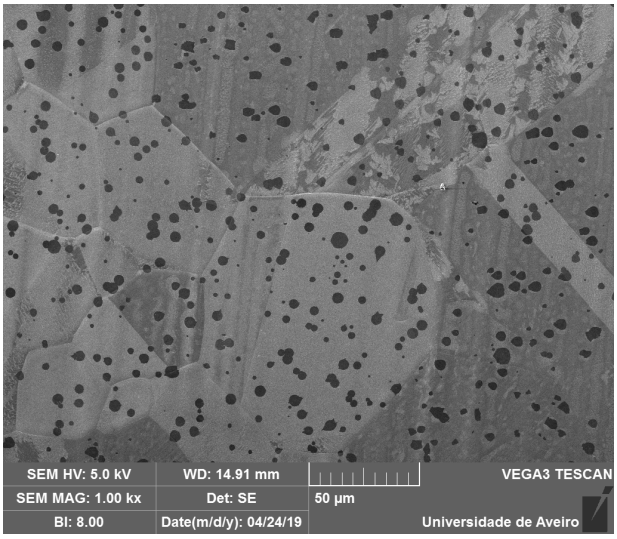

a.

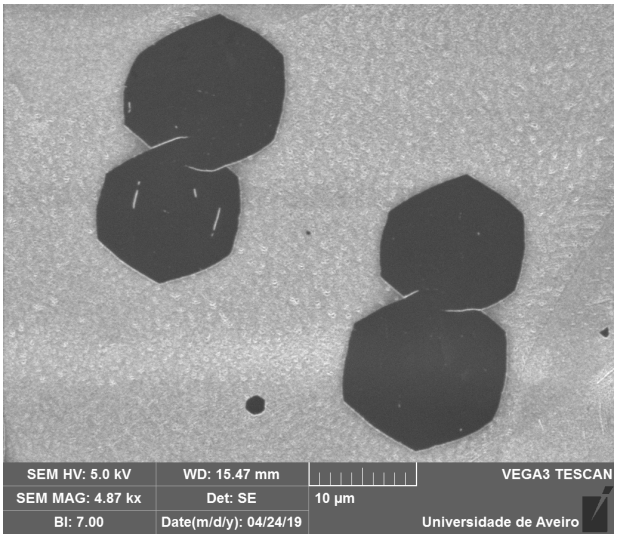

b.

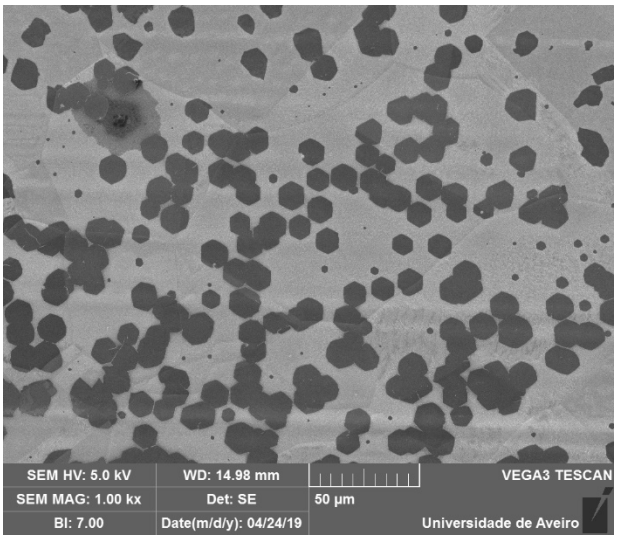

c.

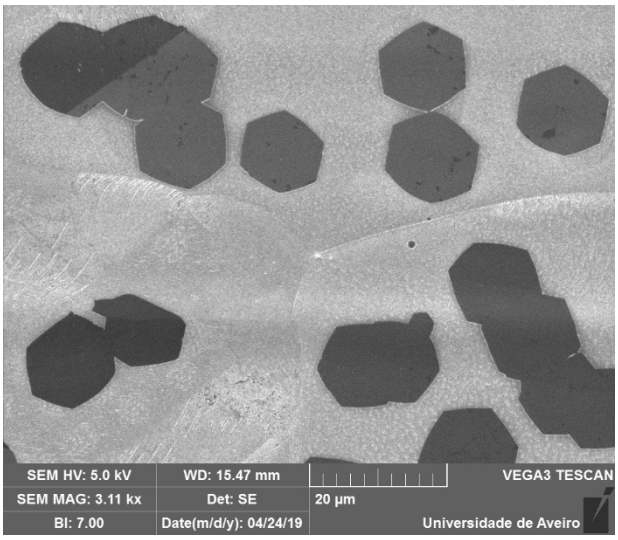

d.

Figure VI-3 shows SEM images of sample 7 (a.) and sample 8 (b. to d.). On this images, insites about the nucleation phases, location, dessity, and GrD coalescence can be collected.

VII. Conclusions

An inductive-based CVD setup was successfully designed and tested with the objective of growing single layer graphene on copper substrates. The work involved the project, the prototype, the construction and the optimization of the circuitry, which is composed by the setup and temperature calibration, crucial parameters to correct PID control.

The developed setup allowed the synthesis of well-defined polygonal hexagons of single crystal graphene domains in short runs, that constitutes an added value taking advantage of the low thermal inertia of the proposed deposition concept. Raman spectroscopy and SEM imaging put in evidence the high quality of graphene domains, despite the high anisotropic degree, indicating that the GrD growth takes place out of epitaxial regime. Moreover, more work should be done in the deposition process to reduce nucleation sites and increase the overall size of the graphene crystals.

In terms of future work, several limiting factors which constrained the circuit implementation along the building process must be surpassed to improve it. An improvement can be done to reduce the circuit power losses and implement a magnetic shield to the coil in order to increase the magnetic field density at the hot zone, to eliminate the susceptor heat diffusion, and attaining successful depositions in the freestanding sample arrangement. Other coil arrangement should be also tested in order to improve the temperature distribution over the sample.

Other factors considered to be good guiding routes were given by the experiments on NiCu samples, indicating that there are advantages in the use of both materials for the catalytic process of graphene deposition, but a close control of the Ni distribution on the Cu bulk must be done. In addition, the temperature gradient characterization should be conducted in samples with higher dimensions in order to understand the ability of the system in a wafer size or roll-to-roll applications.

Another important improvement to be explored could be the introduction of fresh precursor delivery close to the growth region by a local 'shower' or needle tube, an approach already validated by other groups. This seems an advantage when combined with a localized heat source such as that here proposed and has good indications to increase the control over the depositing reacting phases.

To achieve pristine high quality graphene using the CVD technique is not a trivial task, as evidenced by the uncountable published results over the world. Nonetheless, this work allowed to explore the main involved variables to increase control of the different deposition steps, along with the identification of the typical difficulties inherent to such a multidisciplinary challenge.

References

[1] L. Baraton *et al.*, "On the mechanisms of precipitation of graphene on nickel thin films," *EPL - Europhys. Lett.*, vol. 96, p. 46003, 2011.

[2] G. K. and M. T. Additional, "Fundamentals of Chemical Vapor Deposited Graphene and Emerging Applications," *IntechOpen*, p. 13, 2016.

[3] L. Adamska, Y. Lin, A. J. Ross, M. Batzill, and I. I. Oleynik, "Atomic and electronic structure of simple metal/graphene and complex metal/graphene/metal interfaces," *Phys. Rev. B - Condens. Matter Mater. Phys.*, vol. 85, no. 19, pp. 1–8, 2012.

[4] Y. Liu *et al.*, "How Low Nucleation Density of Graphene on CuNi Alloy is Achieved," *Adv. Sci.*, vol. 5, no. 6, 2018.

[5] A. Van Der Drift, "Evolutionary Selection, a Principle Governing Growth Orientation in Vapour-Deposited Layers," *Philips Res. Repts*, vol. 22, pp. 267–288, 1967.

[6] T. Wu *et al.*, "Fast growth of inch-sized single-crystalline graphene from a controlled single nucleus on Cu-Ni alloys," *Nat. Mater.*, vol. 15, no. 1, pp. 43–47, 2016.

[7] T. Wu *et al.*, "Fast growth of inch-sized single-crystalline graphene from a controlled single nucleus on Cu-Ni alloys (Supplementary)," *Nat. Mater.*, vol. 15, no. 1, pp. 43–47, 2016.

[8] S. Chen *et al.*, "Synthesis and Characterization of Large-Area Graphene and Graphite," *Nano Lett.*, pp. 3519–3525, 2011.

[9] I. V. Vlassiouk *et al.*, "Evolutionary selection growth of two-dimensional materials on polycrystalline substrates," *Nat. Mater.*, vol. 17, no. 4, pp. 318–322, 2018.

[10] P. C. Rogge, K. Thürmer, M. E. Foster, K. F. McCarty, O. D. Dubon, and N. C. Bartelt, "Real-time observation of epitaxial graphene domain reorientation," *Nat. Commun.*, vol. 6, pp. 6–11, 2015.

[11] J. Hu *et al.*, "Roles of oxygen and hydrogen in crystal orientation transition of copper foils for high-quality graphene growth," *Sci. Rep.*, vol. 7, no. February, pp. 1–9, 2017.

[12] T. H. R. Cunha, J. Ek-Weis, R. G. Lacerda, and A. S. Ferlauto, "Graphene chemical vapor deposition at very low pressure: The impact of substrate surface self-diffusion in domain shape," *Appl. Phys. Lett.*, vol. 105, no. 7, pp. 1–6, 2014.

[13] T. Taira, S. Obata, and K. Saiki, "Nucleation site in CVD graphene growth investigated by radiation-mode optical microscopy," *Appl. Phys. Express*, vol. 10, no. 5, 2017.

[14] A. Dahal and M. Batzill, "Graphene-nickel interfaces: A review," *Nanoscale*, vol. 6, no. 5, pp. 2548–2562, 2014.

[15] U. Narula and C. Tan, "Determining the Parameters of Importance of a Graphene Synthesis Process Using Design-of-Experiments Method," *Appl. Sci.*, vol. 6, no. 7, p. 204, 2016.

[16] K. M. Omambac *et al.*, "Temperature-Controlled Rotational Epitaxy of Graphene," *Nano Lett.*, 2019.

[17] C. HU, H. SHEN, S. ZHANG, and H. LI, "Methane pyrolysis in preparation of pyrolytic carbon: Thermodynamic and kinetic analysis by density functional theory," *Chinese J. Aeronaut.*, pp. 9–11, 2019.

[18] J. Hrbek, "Induction heating of thin nonmagnetic sheets in transverse time-variablemagnetic field," *Acta Tech. CSAV (Ceskoslovensk Akad. Ved)*, vol. 60, no. 1, pp. 15–29, 2015.

[19] M. C. Marinica, C. Barreteau, D. Spanjaard, and M. C. Desjonquères, "Diffusion rates of Cu adatoms on Cu(111) in the presence of an adisland nucleated at fcc or hcp sites," *Phys. Rev. B - Condens. Matter Mater. Phys.*, vol. 72, no. 11, 2005.

[20] M. R. Calvo *et al.*, "Activation Energy Paths for Graphene Nucleation and Growth on Cu," *ACS Nano*, vol. 6, no. 4, pp. 3614–3623, 2012.

[21] R. S. Weatherup *et al.*, "In Situ Graphene Growth Dynamics on Polycrystalline Catalyst Foils," *Nano Lett.*, vol. 16, no. 10, pp. 6196–6206, 2016.

[22] M. H. Ani *et al.*, "A critical review on the contributions of chemical and physical factors toward the nucleation and growth of large-area graphene," *J. Mater. Sci.*, vol. 53, no. 10, pp. 7095–7111, 2018.

[23] S. M. Kim *et al.*, "The effect of copper pre-cleaning on graphene synthesis," *Nanotechnology*, vol. 24, no. 36, 2013.

[24] A. Scientific, “Nitric Acid, 3M, Safety data sheet,” pp. 1–6, 2015.

[25] A. Scientific, “Acetic Acid,ACS, Safety Data Sheet,” pp. 1–8, 2015.

[26] A. Prakash, J. G. Jency, and M. C. Mathew, “A Review of various Wet Etching Techniques used in Micro Fabrication for Real Estate Consumption,” *Int. J. Comput. Appl.*, pp. 975–8887, 2013.

[27] K. P. Sharma, G. Kalita, and M. Tanemura, “Influence of Copper Crystallographic orientation on Growth and Etching of graphene,” *Conf. Pap.*, vol. 9A-3–4, no. November, pp. 2–4, 2016.

[28] J. Y. Kim, J. A. Rodriguez, J. C. Hanson, A. I. Frenkel, and P. L. Lee, “Reduction of CuO and Cu2O with H2: H embedding and kinetic effects in the formation of suboxides,” *J. Am. Chem. Soc.*, vol. 125, no. 35, pp. 10684–10692, 2003.

[29] M. S. Kim, J. M. Woo, D. M. Geum, J. R. Rani, and J. H. Jang, “Effect of copper surface pre-treatment on the properties of CVD grown graphene,” *AIP Adv.*, vol. 4, no. 12, pp. 0–8, 2014.

[30] K. P. Sharma, S. M. Shinde, M. S. Rosmi, S. Sharma, G. Kalita, and M. Tanemura, “Effect of copper foil annealing process on large graphene domain growth by solid source-based chemical vapor deposition,” *J. Mater. Sci.*, vol. 51, no. 15, pp. 7220–7228, 2016.

[31] J. Pang *et al.*, “Oxidation as a means to remove surface contaminants on Cu foil prior to graphene growth by chemical vapor deposition,” *J. Phys. Chem. C*, vol. 119, no. 23, pp. 13363–13368, 2015.

[32] P. Heitjans and J. Kärger, *Diffusion in condensed matter: Methods, materials, models*, no. April. 2005.

[33] T. Taira, S. Obata, and K. Saiki, “Effect of grain boundaries in Cu foil on CVD growth of graphene,” *Appl. Phys. Express*, vol. 10, no. 7, pp. 8–11, 2017.

[34] P. Li, Z. Li, and J. Yang, “Dominant Kinetic Pathways of Graphene Growth in Chemical Vapor Deposition: The Role of Hydrogen,” *J. Phys. Chem. C*, vol. 121, no. 46, pp. 25949–25955, 2017.

[35] A. B. Phillips and B. S. Shivaram, “High capacity hydrogen absorption in transition metal-ethylene complexes observed via nanogravimetry,” *Phys. Rev. Lett.*, vol. 100, no. 10, 2008.

[36] M. Lagos and I. K. Schuller, “Kinetics ofhydrogen absorption in transition metals and subsurface bonding,” *Surf. Sci.*, vol. 138, no. 2–3, pp. 5979–5981, 1984.

[37] M. Losurdo, M. M. Giangregorio, P. Capezzuto, and G. Bruno, “Graphene CVD growth on copper and nickel: Role of hydrogen in kinetics and structure,” *Phys. Chem. Chem. Phys.*, vol. 13, no. 46, pp. 20836–20843, 2011.

[38] I. Vlassiouk *et al.*, “Graphene nucleation density on copper: Fundamental role of background pressure,” *J. Phys. Chem. C*, vol. 117, no. 37, pp. 18919–18926, 2013.

[39] P. Li, Z. Li, and J. Yang, “Dominant Kinetic Pathways of Graphene Growth in Chemical Vapor Deposition: The Role of Hydrogen. (arXiv:1711.02244v1 [cond-mat.mtrl-sci]),” pp. 1–18.

[40] M. Sarno, G. Rossi, C. Cirillo, and L. Incarnato, “Cold Wall Chemical Vapor Deposition Graphene-Based Conductive Tunable Film Barrier,” *Ind. Eng. Chem. Res.*, vol. 57, no. 14, pp. 4895–4906, 2018.

[41] P. M. Martin, *Handbook of Depositions Tecnologies for film and coating.* 2005.

[42] G. Faggio *et al.*, “High-temperature growth of graphene films on copper foils by ethanol chemical vapor deposition,” *J. Phys. Chem. C*, vol. 117, no. 41, pp. 21569–21576, 2013.

[43] R. Muñoz and C. Gómez-Aleixandre, “Review of CVD synthesis of graphene,” *Chem. Vap. Depos.*, vol. 19, no. 10–12, pp. 297–322, 2013.

[44] J. H. Cho, J. J. Gorman, S. R. Na, and M. Cullinan, “Growth of monolayer graphene on nanoscale copper-nickel alloy thin films,” *Carbon N. Y.*, vol. 115, pp. 441–448, 2017.

[45] M. Faisal *et al.*, “Cold Wall CVD (CWCVD) in the Synthesis of Few Layered Graphene on Ni,” *pikajha@sspl.drdo.in (P.J.); anil_spl@yahoo.co.in (A.A.); pkchaudhury@sspl.drdo.in (P.K.C.)*, no. May, pp. 1–9, 2017.

[46] C. M. Seah, S. P. Chai, and A. R. Mohamed, “Mechanisms of graphene growth by chemical vapour deposition on transition metals,” *Carbon N. Y.*, vol. 70, pp. 1–21, 2014.

[47] S. Das and J. Drucker, “Nucleation and growth of single layer graphene on electrodeposited Cu by cold wall chemical

vapor deposition," *Nanotechnology*, vol. 28, no. 10, 2017.

[48] Z. Sun, Z. Yan, J. Yao, E. Beitler, Y. Zhu, and J. M. Tour, "Growth of graphene from solid carbon sources," *Nature*, vol. 468, no. 7323, pp. 549–552, 2010.

[49] R. Piner *et al.*, "Graphene synthesis via magnetic inductive heating of copper substrates," *ACS Nano*, vol. 7, no. 9, pp. 7495–7499, 2013.

[50] Z. Zhang *et al.*, "The Way towards Ultrafast Growth of Single-Crystal Graphene on Copper," *Adv. Sci.*, vol. 4, no. 9, 2017.

[51] J. Ryu, Y. Kim, D. Won, N. Kim, J. S. Park, and E. Lee, "Fast Synthesis of High-Performance Graphene by Rapid Thermal Chemical Vapor Deposition (supplementary)," *ACS Nano*, vol. 8, no. Xx, pp. 950–956, 2014.

[52] G. Sinha and S. S. Prabhu, "Analytical model for estimation of eddy current and power loss in conducting plate and its application," *Physical Review Special Topics - Accelerators and Beams*, vol. 14, no. 6, pp. 1–10, 2011.

[53] COMSOL Multiphysics, "AC / DC Module User ' s Guide," *Manual*, p. 221, 2017.

[54] R. A. Matula, "Electrical Resistivity of Copper, Gold, Palladium and Silver." Certer for Information and Numerical Data Analysis and Synthesis.

[55] E. Paw, T. Resistance, and E. Paw, "Resistivity of tungsten as a function of temperature," vol. 1069, no. July 1926, pp. 202–207, 2004.

[56] R. E. Haimbaugh, *Practical Induction Heat Treating*. 2001.

[57] COMSOL Multiphysics, *Heat Transfer Module*. 2015.

[58] J. G. Hust and A. B. Lankford, "Thermal Conductivity of Aluminum, Copper, Iron and Tungsten for Temperatures From 1 K To the Melting Point," no. June, 1984.

[59] J. P. Holman, *Heat Transfer (10th Edition)*. 2010.

[60] J. Zhang, Y. Huang, Y. Liu, and Z. Wang, "Direct diffusion bonding of immiscible tungsten and copper at temperature close to Copper's melting point," *Mater. Des.*, vol. 137, pp. 473–480, 2018.

[61] O. M. Necati, "Heat Transfer: A Basic Approach." McGraw-Hill Book Company, p. 744, 1985.

[62] H. M. Lyon, *Boundary Layer Theory*, vol. 7, no. 2. 2014.

[63] J. R. Howell, R. Siegel, and M. P. Mengüç, *Thermal Radiation Heat Transfer, 5th Edition*. 2010.

[64] H. Watanabe, M. Susa, and K. Nagata, "Discontinuity in normal spectral emissivity of solid and liquid copper at the melting point," *Metall. Mater. Trans. A Phys. Metall. Mater. Sci.*, vol. 28, no. 12, pp. 2507–2513, 1997.

[65] K. G. Ramanathan and S. H. Yen, "High-temperature emissivities of copper, aluminum, and silver," *J. Opt. Soc. Am.*, vol. 67, no. 1, p. 32, 1976.

[66] D. P. Verret and K. G. Ramanathan, "Total hemispherical emissivity of tungsten," *J. Opt. Soc. Am.*, vol. 68, no. 9, p. 1167, 1977.

[67] IllinoisCapacitor, "Datasheet, LC4 High Power Resonant Capacitors."

[68] Raytek, "Marathon MR Operating Instructions," 2011.

[69] P. D. Foote, "The total emissivity of platinum and the relation between total emissivity and resistivity," *Phys. Rev.*, vol. 4, no. 6, p. 550, 1914.

[70] Texas Instruments, "CD4046B," no. July, pp. 6–8, 2003.

[71] I. Power, M. Signal, and C. Devices, "Tlp2955," pp. 1–11, 2016.

[72] P. Instrumentation, D. Acquisition, T. Equipment, P. A. Equipment, T. Amplifiers, and R. H. Equipment, "OPA27 Ultra-Low Noise , Precision OPERATIONAL AMPLIFIERS," *Current*, 2005.

[73] C. Gokqek, "Tracking the Resonance Frequency of a Series RLC Circuit Using a Phase Locked Loop," no. 1.

[74] B. Carter and T. Brown, "Handbook of operational amplifier applications," *Texas Instruments Appl. Rep.*, no. September, pp. 1–94, 2001.

[75] Micrometals, “PC Series - Power Conversion & Line Filter Applications,” no. L, p. 72, 2007.

[76] Analog Devices, “ADUM7234 - Isolated , Precision Half-Bridge Driver , 4 A Output,” 2013.

[77] D. K. Morgan, “CD4046B Phase-Locked Loop : A Versatile Building Block for Micropower Digital and Analog Applications,” no. February, pp. 1–24, 2003.

[78] Analog Devices, “ADuM3223 Evaluation Board User Guide,” pp. 1–8, 2009.

[79] L. H. Dixon, “Section 4: Power Transformer Design,” *TI Magn. Des. Handb.*, pp. 31–40, 2000.

[80] R. semiconductor, “RFUS20TM6S - Super Fast Recovery Diode,” 2016.

[81] D. Sheet, “ADuM3223 Isolated Precision Half-Bridge Driver,” 2012.

[82] Infineon Technologies AG, “Ikw40N120H3,1200V high speed switching series third generation,” *Datasheet*, pp. 1–17.

[83] M. I. L. Std and J. Sae, “7796 AC / DC Power Amplifier 7796 Voltage Potential,” pp. 1–4.

[84] Texas Instruments, “AN-1197 Selecting Inductors for Buck Converters,” no. May 2001, pp. 1–18, 2013.

[85] S. Jiao, W. Song, and X. Feng, “Filter parameter optimization design of single-phase LCL-type three-level rectifier equipped in train for high-speed-railway harmonic resonance suppression,” *2016 IEEE 8th Int. Power Electron. Motion Control Conf. IPEMC-ECCE Asia 2016*, vol. 2, pp. 2589–2593, 2016.

[86] P. Trinsoutrot, C. Rabot, H. Vergnes, A. Delamoreanu, A. Zenasni, and B. Caussat, “High quality graphene synthesized by atmospheric pressure CVD on copper foil,” *Surf. Coatings Technol.*, vol. 230, pp. 87–92, 2013.

[87] H. Systems, “7548/7794/7796,” no. 65.

[88] “User’s manual FLIR A3xx series,” *Arbeit*, no. 110, 2009.

[89] M. S. Kim, J. M. Woo, D. M. Geum, J. R. Rani, and J. H. Jang, “Effect of copper surface pre-treatment on the properties of CVD grown graphene,” *AIP Adv.*, vol. 4, no. 12, pp. 0–8, 2014.

[90] K. G. Ramanathan, S. H. Yen, and E. A. Estalote, “Total hemispherical emissivities of copper, aluminum, and silver,” vol. 16, no. 11, 1977.

[91] P. Franke and D. Neuschütz, “Ni-W,” in *Binary Systems. Part 4: Binary Systems from Mn-Mo to Y-Zr: Phase Diagrams, Phase Transition Data, Integral and Partial Quantities of Alloys*, P. Franke and D. Neuschütz, Eds. Berlin, Heidelberg: Springer Berlin Heidelberg, 2006, pp. 1–3.

[92] B. Predel, “Cu-Ni (Copper-Nickel),” in *Cr-Cs -- Cu-Zr*, O. Madelung, Ed. Berlin, Heidelberg: Springer Berlin Heidelberg, 1994, pp. 1–7.

[93] K. T. Datasheet, “Chatalog - Sintec Ceramics, Paints and Sprays,” p. 1, 2018.

[94] H. Zhang, S. Yao, and M. Widom, “Predicted phase diagram of boron-carbon-nitrogen,” *Phys. Rev. B*, vol. 93, no. 14, pp. 1–9, 2016.

[95] X.-T. Y. C. Xu, Yongdong, *Chemical Vapour Deposition: An Integrated Engineering Design for Advanced Materials*, vol. 1. Springer, 2010.

[96] A. C. Ferrari and D. M. Basko, “Ramatile tool for studying the properties of graphene.,” *Nat. Nanotechnol.*, vol. 8, no. 4, pp. 235–46, 2013.

[97] V. Zólyomi, J. Koltai, and J. Kürti, “Resonance Raman spectroscopy of graphite and graphene,” *Phys. Status Solidi Basic Res.*, vol. 248, no. 11, pp. 2435–2444, 2011.

Annex

1. Sample Lichtenberg pattern cut evolution

During de deposition process, the induced high temperatures sometimes lead to sample deterioration, resulting in the growth of a Lichtenberg like pattern from the middle of one of the sample edges and slowly progressing through the sample length. During this event, the power consumption also increases, leading to the assumption that the net sample temperature also decreases and the control PID tries to balance it.

A simulation in COMSOL Multiphysics, with the same boundary conditions used for the simulation presented in Electromagnetic simulation chapter, was used to investigate this phenomenon. From Figure 0-1, it can be seen from the evolution of the temperature distribution pattern that the hottest site is located in the cut tip surroundings, allowing for this material to attain conditions that leads to evaporation, further expanding the cut pattern. Figure 0-1 (a) to (e) can be related to the samples, as for Figure 0-1 (f) to (h) can explain the evolution pattern seen in samples, since the hottest site stays located near the sample centre.

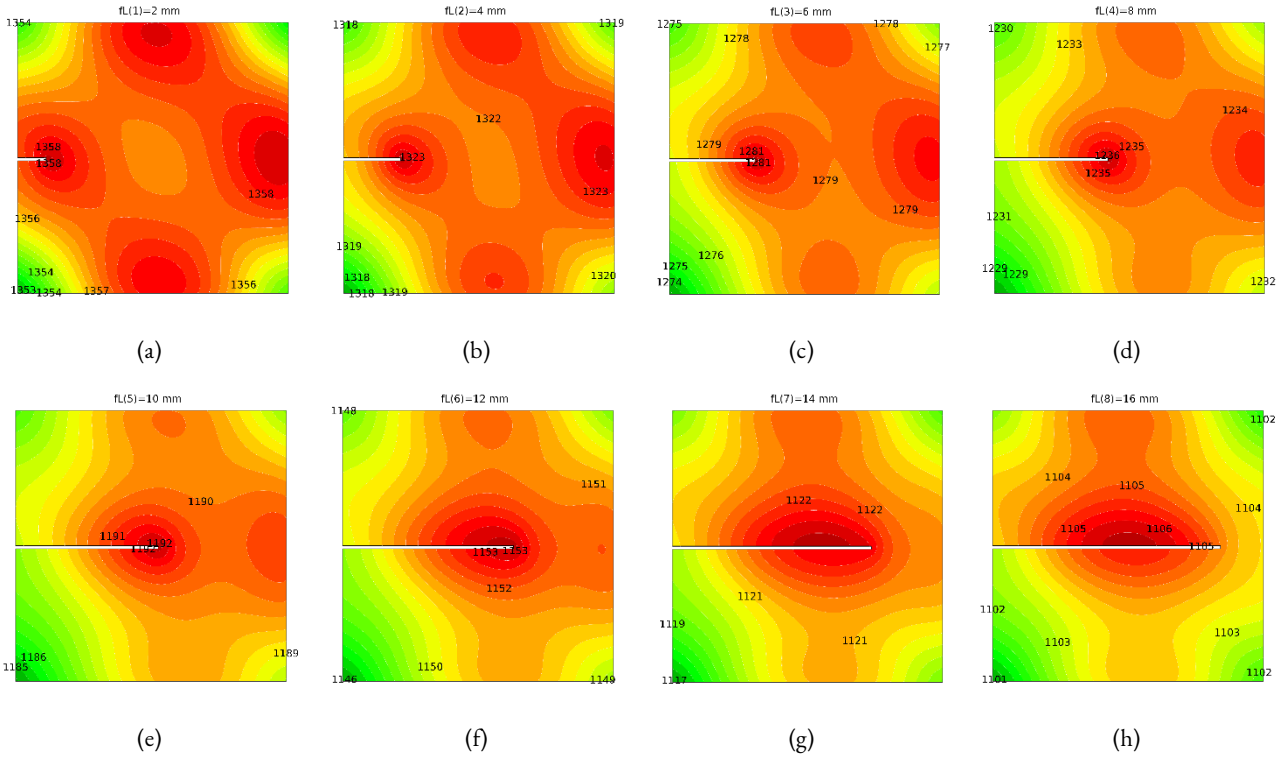

Figure 0-1: Temperature variation on the sample as a function of the fringe length evolution. The color legend magnitude is relactive to each individual figure, the maximum and minimum temperatures should be read from each figure also.

To understand the reason for this behaviour, the current density distribution can be observed in Figure 0-2. From comparing the current density distribution scales between Figure 0-2.a and .b, it is noticeable that the case where the cut has 16mm, the induced currents are distributed more uniformly, almost as in two independent pieces of material were placed in between the coils. As for in the beginning of the cut development, the current density distribution is concentrated on the fringe front (.c), resulting in the temperature differences stated above.

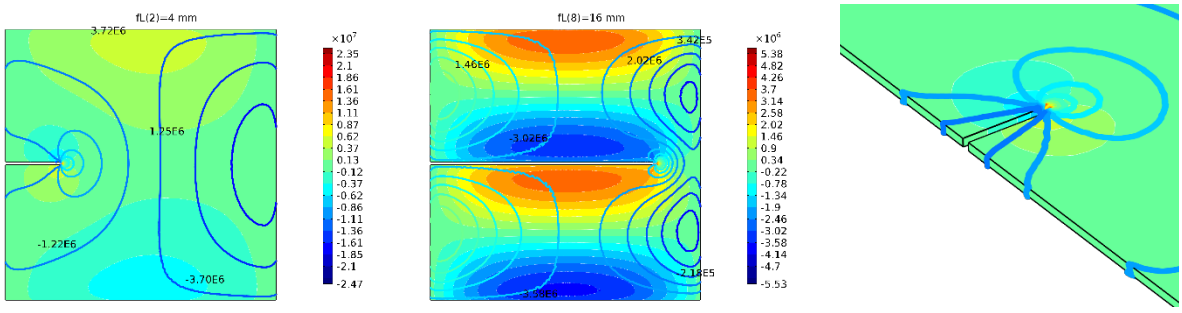

(a) (b) (c)

Figure 0-2: Current distribution contours .a for a 4mm cut in the sample; .b for a 16mm cut on the sample and .c a close up of the current density maximum zone, situated on the cut front for a 2mm cut.

2. Long non-square sample

In the long sample simulation, for this coil, the temperature has a parabolic distribution along the sample length, reaching a maximum gradient of 119 K between hot and cold extremes. In a roll to roll setup, this can be advantageous to restrict the hot zone of a reactor.

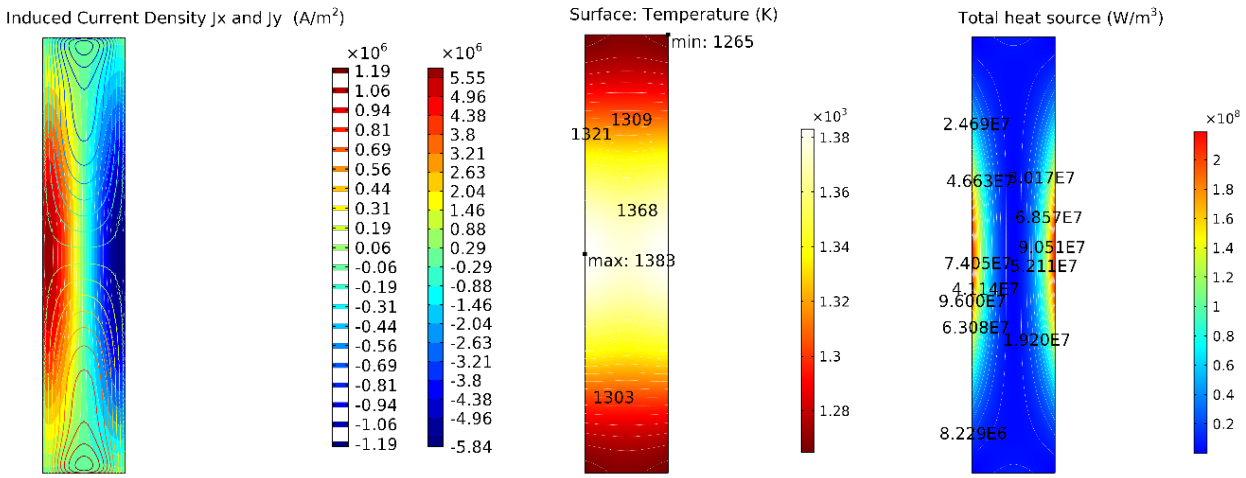

(a) (b) ©

Figure 0-3: simulation results for the 100mm non square sample with its centre concentric with the coil. .a induced current density distribution; .b the temperature distribution and .c the total heat resulted from the eddy currents interaction with the material.

3. Circuit simulation

As a crucial understanding tool, a simulation of the circuit was built in MatLab using its Simulink platform. It allowed to easily iterate between different circuit approaches and understand the effect of the available components to decide about the best possible topology to be built with lower DC ripple current, good system response and signal conditioning.

The generic circuit can be seen in Figure 0-4a, along with the represented main probes, which were complemented with the waveform tracing of the different components played a main role on their value choice.

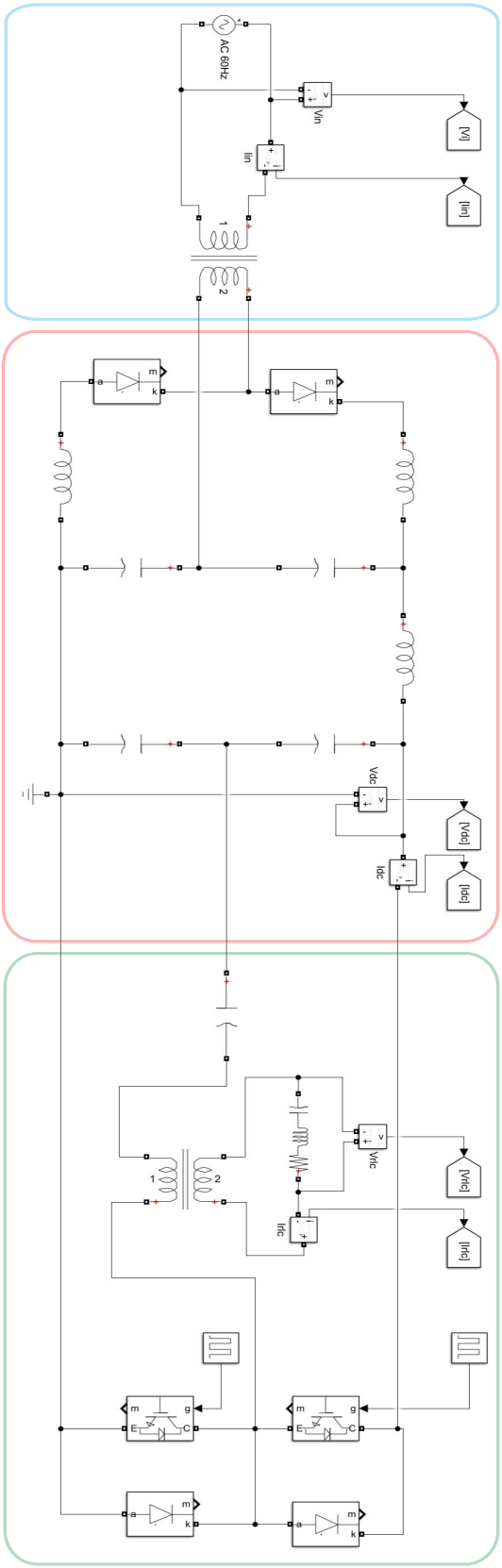

Figure 0-4: (a) Final simulation, accounting for the different parts of the system. In blue the AC power supply and elevator input transformer, in red the VMR including the two 2nd order LC filters and in green, the VDR, simulated with an input gate signal of 80kHz at 0.45 DC, coupled throught the step down transformer to the RLC load.

4. Control program

The control program was developed in LabView, Figure 0-5, it includes an input from the pyrometer reading, a PID and autotune cycle, and an analogue signal output rated from 0~10V, which connects to the PA.

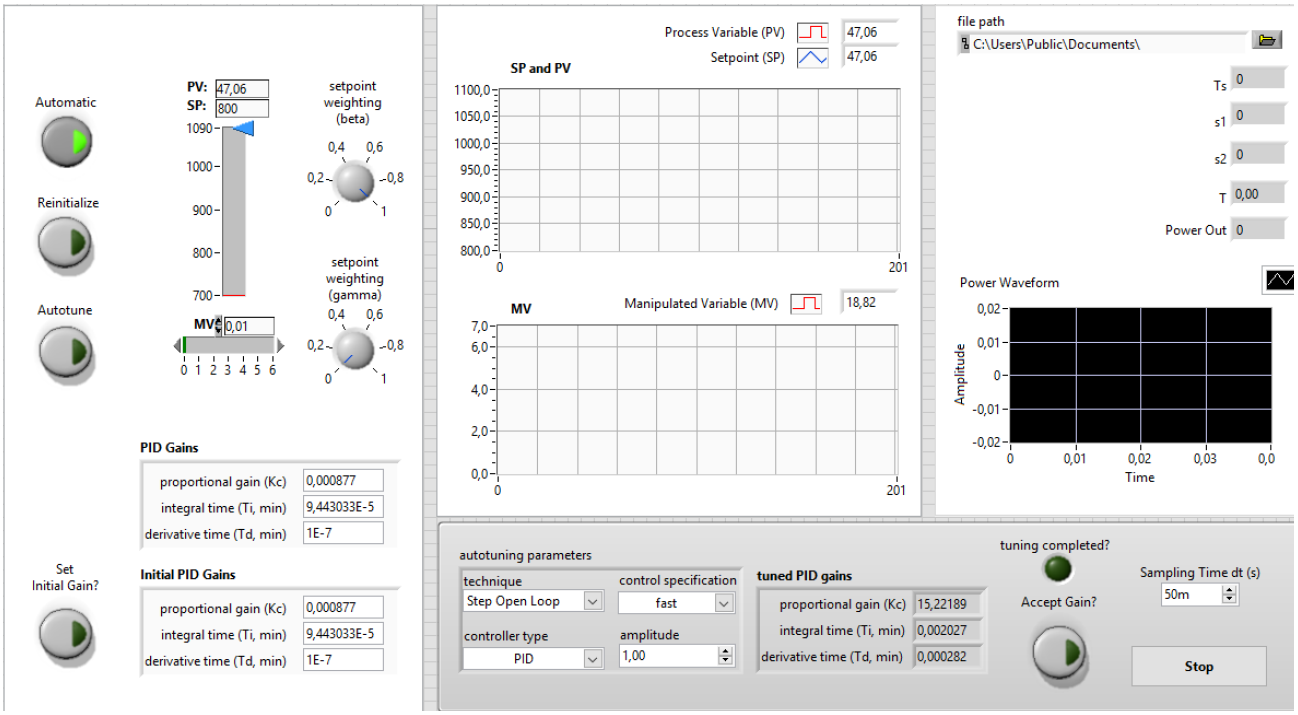

Figure 0-5: Control program user interface. On the left division are the input controls for the temperature setpoint (SP), output signal amplitude (MV), PID gains and the buttons to switch from manual (default) to automatic mode as well as autotune. On the central screen, the reading temperature and setpoint temperatures are dynamically plotted as well as the output signal amplitude. The right screen agglomerates the pyrometer temperature log file, and the output current waveform. The bottom rectangle is the tuning area, where the PID parameters can be adjusted for autotuning; the sampling rate time and an emergency stop button which as pressed will immediately interrupt the automatic cycle and turn the PA input to zero.

It allows the control of the output amplitude signal through direct manual input, and through setpoint temperature, which changes the program to the PID loop. Four kinds of PID loop tuning are allowed as well as a manual input of the proportional, integrate and derivative values. Allowing also to work in PI or P modes as well. The sampling mode can be controlled, but is dependent on the pyrometer sampling mode, with is 1sample/s [68]. Nonetheless a smaller sampling rate was adopted to force the program input to be a moving average of the temperature reading, turning it less sensitive to anomalous readings.

The control program block diagram can be seen in annex 5.

5. Control program block diagram

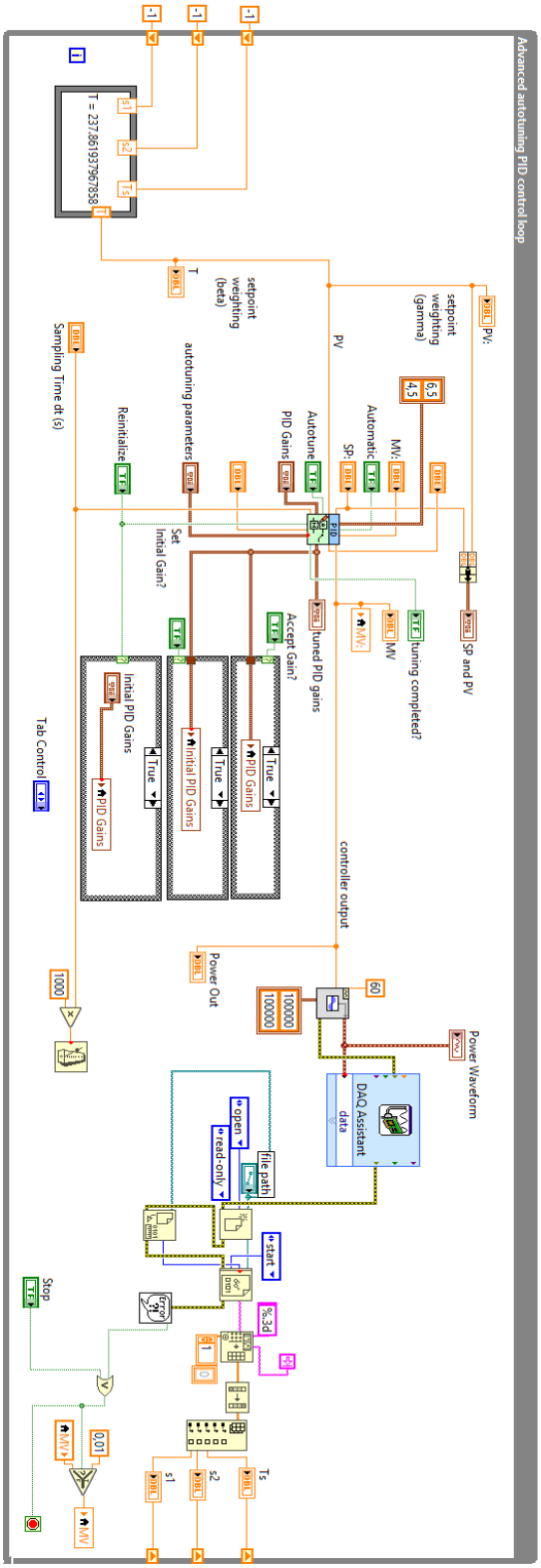

Figure 0-6: Control program block diagram assembled in LabView.